

## Bachelor Thesis

# Design and Analysis of Small Scale Angle of Attack Sensors

Spring Term 2018



## Declaration of originality

The signed declaration of originality is a component of every semester paper, Bachelor's thesis, Master's thesis and any other degree paper undertaken during the course of studies, including the respective electronic versions.

Lecturers may also require a declaration of originality for other written papers compiled for their courses.

---

I hereby confirm that I am the sole author of the written work here enclosed and that I have compiled it in my own words. Parts excepted are corrections of form and content by the supervisor.

**Title of work** (in block letters):

**Authored by** (in block letters):

*For papers written by groups the names of all authors are required.*

**Name(s):**

**First name(s):**

With my signature I confirm that

- I have committed none of the forms of plagiarism described in the '[Citation etiquette](#)' information sheet.
- I have documented all methods, data and processes truthfully.
- I have not manipulated any data.
- I have mentioned all persons who were significant facilitators of the work.

I am aware that the work may be screened electronically for plagiarism.

**Place, date**

**Signature(s)**

*For papers written by groups the names of all authors are required. Their signatures collectively guarantee the entire content of the written paper.*



# Contents

<b>Acronyms and Abbreviations</b>	<b>iv</b>
<b>Abstract</b>	<b>v</b>
<b>1 Introduction</b>	<b>1</b>
<b>2 Design</b>	<b>2</b>
2.1 Design Requirements . . . . .	2
2.2 Design Overview . . . . .	3
2.3 Design Choice . . . . .	4
<b>3 Implementation</b>	<b>6</b>
3.1 Basic Assembly . . . . .	7
3.2 Resistive Sensor . . . . .	9
3.3 Magnetic Sensor . . . . .	11
3.4 Capacitive Sensor . . . . .	14
3.5 Positional Calibration Set-up . . . . .	19
3.6 Wind-tunnel Measurement Set-up . . . . .	19
<b>4 Analysis</b>	<b>24</b>
4.1 Test Cases . . . . .	24
4.1.1 Positional Calibration . . . . .	24
4.1.2 Wind-tunnel Tests . . . . .	25
4.2 Resistive Sensor . . . . .	28
4.3 Magnetic Sensor . . . . .	33
4.4 Capacitive Sensor . . . . .	39
<b>5 Summary and Outlook</b>	<b>44</b>
<b>Bibliography</b>	<b>46</b>
<b>A Tools which were used</b>	<b>47</b>

# Acronyms and Abbreviations

AOA	Angle of attack
RC	Radio control
CFRP	Carbon fiber reinforced polymer
ABS	Acrylonitrile butadiene styrene
MDF	Medium-density fibreboard
ADC	Analog-to-digital converter
IC	Integrated circuit
AC	Alternating current
DC	Direct current
PWM	Pulse-width modulation
EMI	Electromagnetic interference
back-EMF	Back electromotive force
SMD	Surface-mount device
CMOS	Complementary metal–oxide–semiconductor
COBS	Consistent Overhead Byte Stuffing
RMSE	Root-mean-square error
ETH	Eidgenössische Technische Hochschule

# Abstract

This thesis concerns itself with the design and analysis of angle of attack sensors. Angle of attack, in this case, is a property of a fixed-wing aircraft that is flying. It's defined as the angle between the chord line of the wing and the incident airflow.

The design part of the thesis defines the use case for small scale RC aircraft and determines the selection of three designs that are analysed in depth. The three designs all involve pivoted vanes that align themselves with the airflow. They differ in the type of rotary encoder which is used: "resistive sensor" with a potentiometer, "magnetic sensor" with a Hall effect sensor and "capacitive sensor" with a variable capacitor.

The analysis aims to determine calibration curves, hysteresis, noise and system delays. The main result is that the magnetic sensor performs better than the other two and meets the requirements satisfactorily.

# Chapter 1

## Introduction

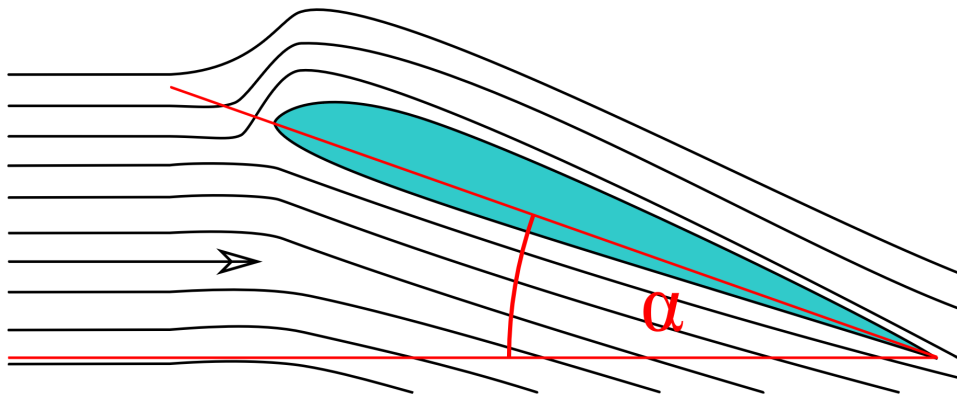


Figure 1.1: Visualisation of angle of attack [1]

Angle of attack (AOA) is the angle between a reference plane (usually through the chord lines of the two wing roots) and a vector representing the relative motion between the aircraft and the surrounding air [2]. The AOA has a strong correlation with the lift force [3], and because of this is a very important dimension for control purposes. Angle of attack sensors can be found on a large variety of aircraft, but are mostly absent from small-scale RC aircraft, as investigations done for this thesis have ascertained. It can be presumed that this is due to low safety requirements for most of these aircraft resulting in a small market for sensors that are compatible with small aircraft. The objective of this thesis is to fill this gap with a reliable and inexpensive sensor.

The thesis will investigate design considerations and analyse performance of a selection of small-scale AOA sensors working with different principles. It is structured in three parts: In the first part existing technology is explored, requirements of the “small-scale” use-case are presented and the scope of this thesis is established. In the second part the design process and construction of the sensors is described together with the design and construction of the measuring and calibrating set-up. In the third part the results of various static and dynamic responses of the sensors are presented, showing the performance of the various sensors. A short summary of these results is found in chapter 5.

# Chapter 2

## Design

### 2.1 Design Requirements

For an AOA sensor design to be considered in this thesis it has to meet specific requirements. It has to be compatible with a 653mm wingspan 380g RC aircraft of the brand *ZOHD Dart*, which will be used as a representative of small-scale RC aircraft. The sensor must also be able to interface with a *Pixhawk* flight-controller, which is used to control the above aircraft. Additional requirements are put in place to guarantee that manufacturing, financial and testing limits are not exceeded:

#### General:

Resolution < 1°	Estimated resolution for usefulness
Range > $\pm 45^\circ$	Estimated max. AOA range during flight
Weight < 20g	Estimated limit based on payload of aircraft
Size < 40x50x100mm	Estimated limit based on size of aircraft
Price < 20 CHF	Price limit based on financial considerations

#### Electronic components:

In stock at digikey.com	Simplification of part search and limitation of shipping costs
Op. Temp. -10° to 40°	Temperatures to be expected during flights
$V_{in}$ 5V or 3V3	Regulated supply voltages of Pixhawk
Non-microscopic	Large enough components for easy handling

#### Mechanical components:

Simple fabrication	No out-of-house manufacturing
In stock at de.misumi-ec.com	Simplification of part search and limitation of shipping costs
Use stainless steel	Rustproof, non-magnetic (see sec. 3.3)

The requirements that rely on estimations are specified by the general operating ranges of small scale fixed-wing aircraft like the one used as reference. To clarify the manufacturing capabilities available in-house, a list of the necessary tools for the fabrication of the sensors is listed in appendix A.

## 2.2 Design Overview

Various methods exist to measure the angle of attack. The primary AOA sensor designs can be subdivided into three main groups with a number of sub groups [4]:

- Pivoted vanes: These are composed of a mass-balanced vane that is free to align itself with the airflow and a rotary encoder fixed to the vane to derive the angle of deflection. This sensor type can be subdivided again in different subcategories based on the type of rotary encoder which is used [5][6]:
  - Absolute / Incremental: Absolute encoders output the current position of the shaft, while incremental encoders output a discrete change in position (and optionally the direction by the use of a quadrature encoder).
  - Discrete / Continuous: Absolute encoders can be subdivided in types that output continuous (analog) values or discrete values in the form of e.g. binary or grey code.
  - Principle: Most of these encoders can be realised by exploiting different physical phenomena. The main four being optical encoders (photo detector + LED), magnetic encoders (hall-effect-sensor plus magnets), capacitive encoders (variable capacitance cap) and resistive encoders (wiper over conductor).
- Differential pressure tubes: These consist of a tube with orifices at different angles on the tip of the tube. The pressure difference between the orifices is a measure of the angle of attack (and airspeed).
- Null-Seeking pressure sensor: These are similar to the differential pressure tube, but instead of measuring the pressure difference, this pressure is used to mechanically align the tube with the airflow. The angle is then measured with a rotary encoder.

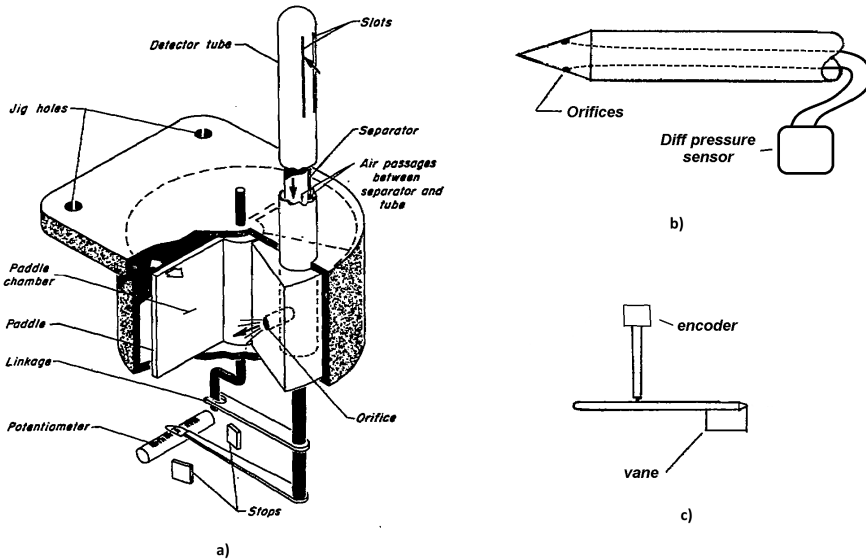


Figure 2.1: Types of angle of attack sensors. a) null-seeking probe b) differential pressure tube c) pivoted vane [4]

Examples of research done on these types of sensors are:

- “Control Strategies for Flight in Extreme Turbulence”[7] using a small scale vane type sensor and a magnetic encoder.
- “Measuring apparent flow vector on a flexible wing kite”[8] using a larger vane type sensor and a magnetic encoder.
- “Simple DIY Angle of Attack (AoA) Indicator”[9] using a small scale vane type sensor and a magnetic encoder.
- “Wind-Tunnel Calibration and Requirements for In-Flight use of fixed hemispherical Head Angle-of-Attack and Angle-of-Sideslip Sensors”[10] using a differential pressure tube.
- “Miniature five-hole pressure probe for measurement of three mean velocity components in low-speed flows”[11] using a small differential pressure tube.
- “Amtek Angle of Attack Transducer”[12] using commercially available vane type sensors and resistive encoder.
- “Aircraft Angle of Attack and Air Speed Detection by Redundant Strip Pressure Sensors”[13] using a form of differential pressure tube where the orifices are on the surface of the wing.

### 2.3 Design Choice

All the designs mentioned in section 2.2 were subsequently evaluated to determine if they could satisfy the design requirements. This evaluation was done only on the basis of the research without any tests or experiments conducted. The following results were found:

- Null-Seeking pressure sensor: No design was found that is simple enough and at the same time small enough to fit in the available space.
- Differential pressure tubes: The complex shape of the tube and the precision required can not be realised with the available manufacturing methods.
- Pivoted vanes: Some types of pivoted vanes can in principle be made to conform with the design requirements. This mainly depends on the rotary encoder used:
  - Absolute / Incremental: Incremental encoders require some form of homing-cycle which is undesirable. Such encoders are for the most part constructed with encoder discs (or equivalents). A disc that provides the required resolution is too expensive respectively too complex to manufacture for this thesis. For these reasons the design selection was restricted to the type of an absolute encoder.
  - Discrete / Continuous: Discrete encoders suffer from the same problems as absolute encoders as they mostly rely on an encoder disc, even if they are realised as incremental encoders. So, the design options were further limited to the type of continuous encoders.
  - Principle: Of the encoder types with the four working principles “optical”, “capacitive”, “magnetic”, “resistive”, all were found to presumably be practicable within the requirements.

In summary, the designs that are to be considered are pivoted vanes based on absolute continuous rotary encoders of the resistive, magnetic, capacitive and optical kind. Since this selection still exceeds the scope of a bachelor thesis it was decided to only focus on three of the four sensors. The optical encoder was discarded because it is regarded as the most difficult to build, the main concerns consisting in interferences caused by sunlight and range problems if a photointerrupter with a moving shield is used. As stated above, it is still thought that such an encoder could meet the requirements. Nevertheless, the sensors that remain to be analysed are therefore of the resistive, magnetic and capacitive designs.

# Chapter 3

## Implementation



Figure 3.1: Final versions of the sensors. Left-to-right: magnetic, resistive, capacitive.

The implementation part of this thesis concerns the technical design process for the three sensors defined in section 2.3. It describes the physical principles exploited by each sensor and how they can be made to correlate with the angle of attack. Part lists and design considerations are included to allow the rebuilding and improvement of the sensors. Additional documents concerning details of the construction process and the tools that were used are listed in the appendix.

This part also describes the design and construction of the measuring and calibration set-up that was built to analyse the performance of the sensors (chapter 4).

### 3.1 Basic Assembly

The basic assembly of all the sensors consists of a wing (2), a swing arm (1) a bearing (5) and a support arm (3). These parts are the same for all three designs to reduce complexity and cost. Figure 3.2 shows the various parts of this structure while the subsequent list describes the individual parts and the requirements they have to fulfil.

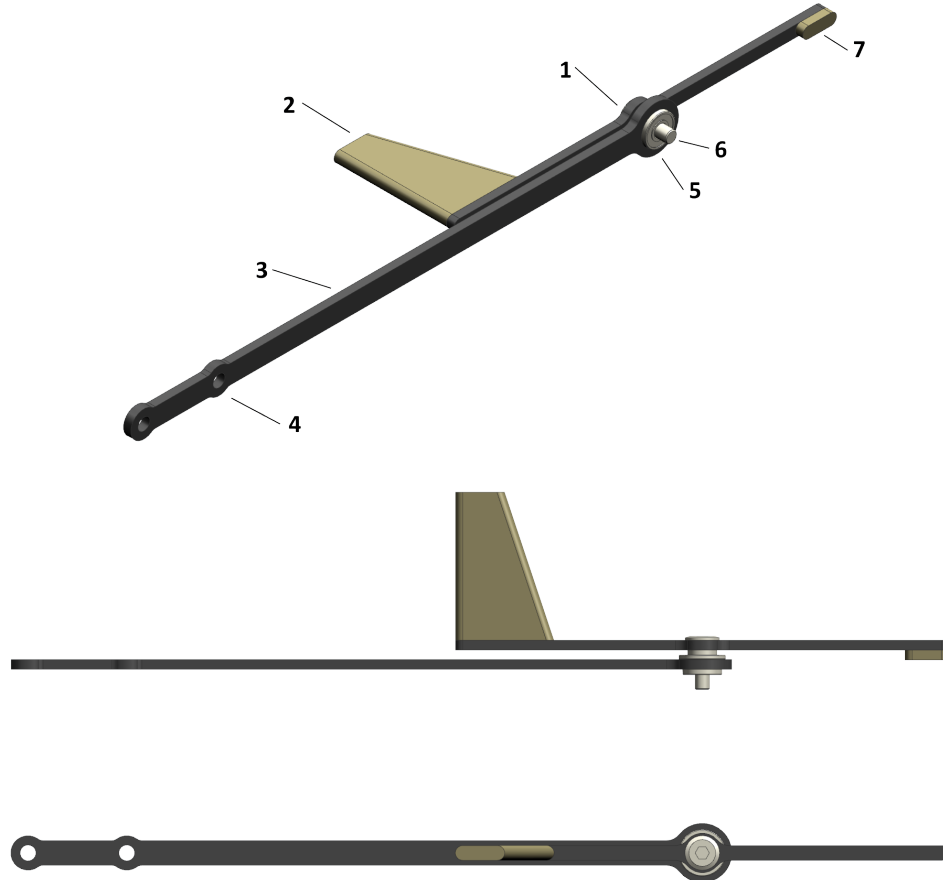


Figure 3.2: Basic assembly - CAD

1. Swing arm: The swing-arm connects the wing (2) and counterweight (7) to the rotation axis (6). It has a mainly structural role, but has to be thin in order not to excessively disturb the airflow in front of the wing. For this reason, a 2mm strong CFRP plate milled to a width of 3mm is used. Thickness and strength are conservatively designed and length is given by the size constraints. Other possible materials were wood, acrylic glass and other plastics that were not as strong as CFRP.
2. Wing: The wing forces the swing-arm (1) to align itself with the airflow. This part has to be as light as possible, as its weight has to be counteracted by the counterweight, and as large as possible, to best react to the airflow. The

material chosen is balsa wood, as it is very light (alternative materials could be wood pulp board or 3D printed ABS). The dimensions are largely dictated by the size constraints. All edges are rounded off to reduce drag and the wing is fixed with instant glue to the roughened-up surface of the swing arm.

3. Support arm: The support arm is used to connect the sensor to the aircraft. Its angle relative to the aircraft defines the 0° AOA line of the aircraft. The non-moving components of the encoder are fixed to it. For simplicity purposes the same 2mm strong CFRP is used as in the swing arm, but with an increased width of 5mm.
4. Mounting holes: The mounting holes are a feature of the support arm and are used to mount the sensor to the aircraft. Two 3mm holes permit a precise and rigid positioning of the sensor.
5. Bearing: The bearing is the element that connects the rotation axis (6) to the support arm (4). In addition to the general requirements it is required to be shielded or sealed, lipped and of reasonable dimensions. These restrictions together with the requirement of being in stock at de.misumi-ec.com led to part C-SFL693ZZ. It has a 3mm inner diameter (adequate for a M3 screw to fit) and is pressure fitted in the support arm and located through its lip.
6. Axis: The axis has to connect the swing arm (1) to the bearing (5) and a future rotary encoder. For a simple construction it was decided to use a combination of a long screw and some washers. The screw has the additional requirement of having a low-profile head so as not to disturb the airflow to the wing. The parts used are (from Misumi): CBSTSE3 screws and WSSB6 washers.
7. Counterweight: The counterweight is fixed to the swing arm (1) opposite to the wing (2). This part is necessary to balance the swing arm thus nullifying the effect of gravity. For this application a material with high density is desirable, as it should not increase the bulk on the tip for aerodynamic reasons. The material used is a piece of a iron nail fixed to the opposing side of the arm to further reduce disturbances to the air in front of the wing.

The basic assembly has been worked out in two steps. In the first step all the components were made of acrylic glass to test the manufacturing capabilities and to get an impression of the size. It was noticed that a lip on the bearing is required to position it consistently and that one bearing would not be sufficient to prevent wobbling of the rotation axis. The second and final step was to built the device with the appropriate materials. No solution to the wobbling problem was found, but it does not appear to be pronounced enough to cause further problems.



Figure 3.3: Steps 1 and 2 of the basic assembly design

### 3.2 Resistive Sensor

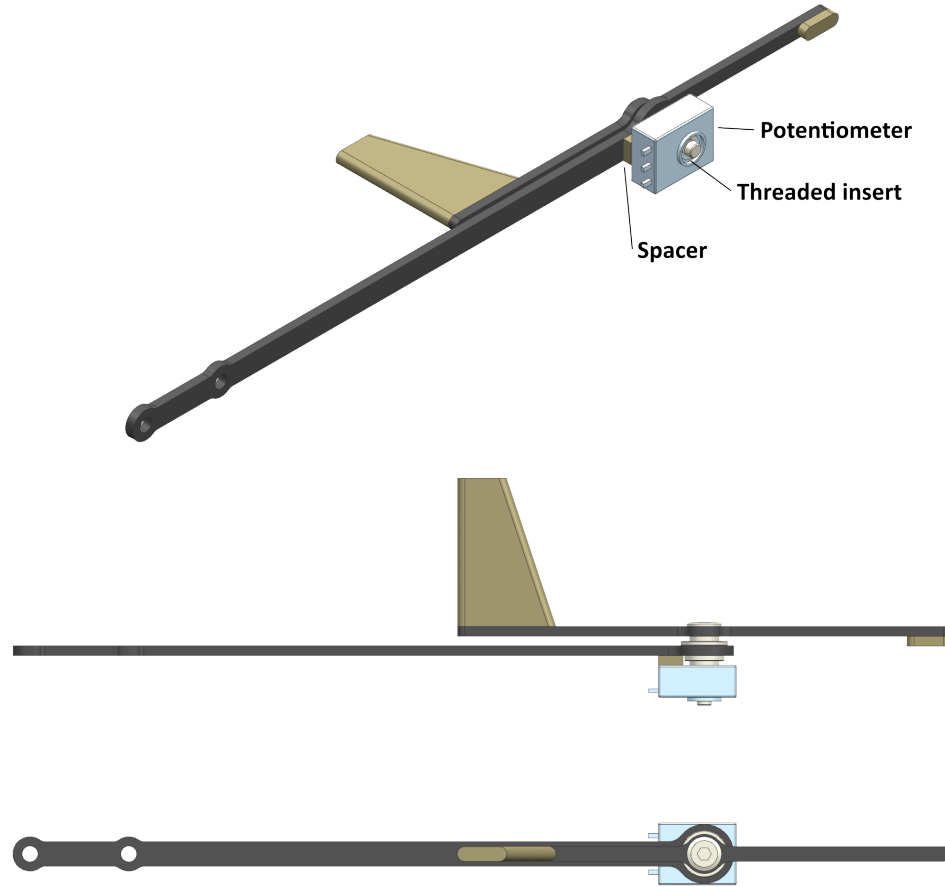


Figure 3.4: Resistive Sensor - CAD

The resistive sensor is based on a resistive rotary encoder. The most common type of such encoders that output continuous absolute values is called potentiometers. A potentiometer works by putting a voltage over a ring-shaped resistive strip. A conductive wiper that rotates with the axis is pushed against that strip. The wiper picks up the voltage at different points of the strip, making it a variable voltage divider. This makes the wiper output voltage directly proportional to the axis angle.

Such potentiometers are widely used and cheap to obtain. For this reason, the resistive design is regarded the simplest solution for an AOA sensor. It does however have the disadvantage that, since the wiper relies on some clamping force to maintain contact with the strip, a considerable amount of friction is involved.

Figure 3.5 shows a sketch of a potentiometer and the calculations that led to the relation between output voltage  $V_{out}$  and input angle  $\alpha$ . The following symbols are used:  $V_{in}$  = input voltage,  $R_{tot}$  = total resistance of the resistive strip,  $\alpha_{rng}$  = range of movement,  $I_{in}$  = current flowing from  $V_{in}$  to Gnd.

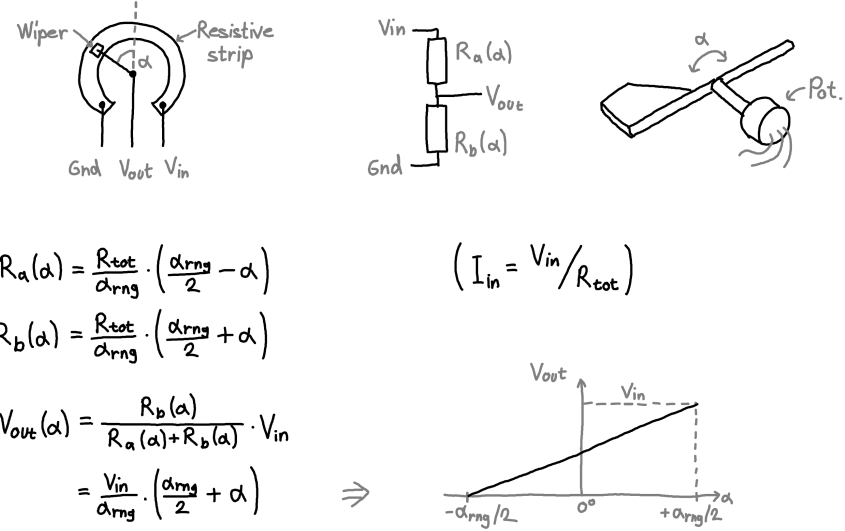


Figure 3.5: Resistive sensor - principle

From the above formulas some requirements for the potentiometer can be deduced. Since  $V_{out \ max} = V_{out}(\alpha_{rng}/2) = V_{in}$  and the ADC of the Pixhawk takes voltages up to 3.3V it follows that  $V_{in} = 3.3V$ . If it is required that  $I_{in} \approx 1mA$  (low power consumption) then  $R_{tot} \approx 3.3k\Omega$ .

With this requirement and the requirement that the potentiometer be mountable to the axis, the best candidate is 4.7k $\Omega$ , 1/5W potentiometer 1624191-4 from TE Connectivity (part nr. A105796-ND at Digikey). This potentiometer has a hole for a D-shaft instead of a knob. By drilling out the hole and inserting a threaded insert (Misumi ENT3-6) it can be affixed to the axis.

This potentiometer possesses a range of  $\alpha_{rng} = 300^\circ$  and the ADC of the Pixhawk, which reads the output voltage, possesses a resolution of 12 bit ( $\Delta V_{out} = 3.3V/2^{12} = 0.8mV$ ). This means that the output curve and resolution are as follows:

$$V_{out}(\alpha) = 0.011 \frac{V}{deg} (150^\circ + \alpha). \quad (3.1)$$

$$\Delta\alpha = \sqrt{\left( \frac{\delta\alpha(V_{out})}{\delta V_{out}} \right)^2 \Delta V_{out}} = 0.07^\circ \quad (3.2)$$

This sensor was the first one to be built. No problems were encountered during manufacturing and the first version was deemed satisfactory. It was possible to moderately decrease the high friction by continuously moving the vane back and forth until the wiper had worked itself in. The remaining friction is regarded as an irresolvable problem for this thesis.



Figure 3.6: Resistive sensor - final product

### 3.3 Magnetic Sensor

The magnetic sensor is based on a magnetic rotary encoder. The most common way to build such an encoder is by fixing a radially polarised magnet to the rotation axis in such a way that the magnetic field strength changes at a fixed point based on the angle of the axis. This magnetic field can be picked up with a Hall effect sensor at that fixed point.

The Hall effect is based on the Lorenz force, according to which a charged particle  $q$  with velocity  $v$  in a magnetic  $B$  and electric  $E$  field experiences a force  $F = qE + qv \times B$ . This relation is exploited by pushing a constant current through a conductor, which causes electrons  $q = -e$  to move with some constant drift speed  $v$ . For the force  $F$  on the electron to be zero (equilibrium), it follows that  $eE = -ev \times B$  where the magnetic field  $B$  is caused by the rotatable magnet. The electric field  $E$  is caused by electrons being pushed to an edge of the conductor by the magnetic field  $B$ . The pushed electrons cause a voltage potential (and thus an  $E$  field) that prevents any more electrons to be pushed to the edge (equilibrium). This voltage potential is the output of the Hall effect sensor (usually with a positive offset to prevent negative voltages for negative magnetic  $B$  fields).

Figure 3.8 shows sketches of a Hall effect sensor, the encoder and the operating principles with equations. For the calculations, the magnet is approximated as a magnetic dipole with dipole moment  $m$ . Other symbols that have not yet been defined are:  $V_H$  Hall voltage,  $V_{H\ Out}$  output voltage of sensor,  $V_{H\ Off}$  offset voltage of sensor,  $s_H$  Hall effect sensitivity,  $s_M$  magnetic sensitivity.

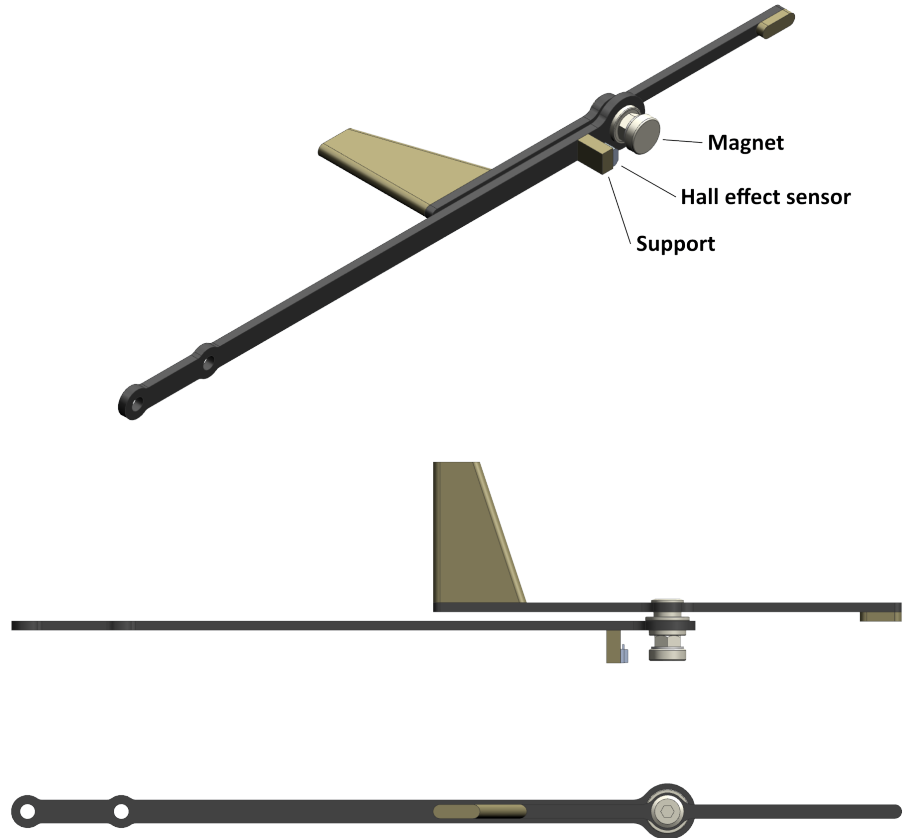


Figure 3.7: Magnetic sensor - CAD

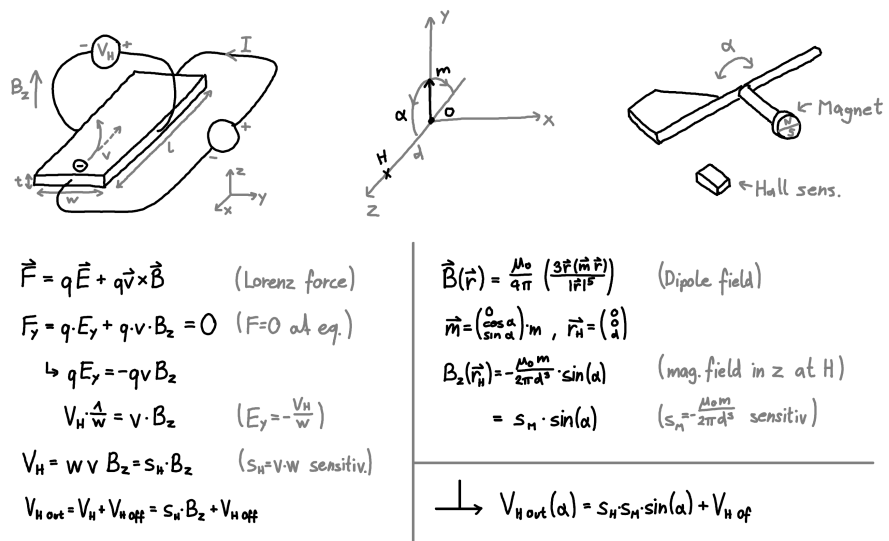


Figure 3.8: Magnetic sensor - principle

A Hall effect sensor can be cheaply bought as an IC and radially polarised magnets are also readily available. This encoder design is the most common for applications where friction is a concern since there are no touching parts.

The requirements of the Hall effect sensor and the magnet are given by the desire to use the full range of output voltages ( $V_{H\ Out}(-45^\circ) = 0V$  and  $V_{H\ Out}(45^\circ) = V_{in}$ ). To accomplish that, an adequate combination of Hall effect sensor, magnet and sensor-magnet distance has to be found. Since there are three unknowns in this combination, the Hall effect sensor and magnet are picked based only on the general requirements and the sensor-magnet distance is chosen in such a way as to be able to use the full output range.

The parts used are magnet “Radial Magnet Inc. 9050” (part nr. 469-1076-ND) and Hall effect sensor “Honeywell SS495A1” (part nr. 480-3591-ND). The sensor-magnet distance that results for these parts is  $d \approx 2.4mm$ . Since this Hall effect sensor takes  $V_{in} = 5V$  a voltage divider is required to feed the output to the Pixhawk’s 3.3V ADC. 330kOhm and 690kOhm resistors are used.

The Hall effect sensor is mounted to the supporting arm through a little piece of balsa wood, instant glue and some shrink tube. The Magnet is fixed to the rotation axis by gluing a nut to a plastic washer and the washer to the magnet. A shrink tube over the magnet is used to provide padding.

For this application it is very important that all metal components be made of non-magnetic materials (like stainless steel in this case) to prevent interactions with the magnet. The bearing used, although marketed as stainless turned out to only possess stainless bearing races but not balls. This causes very slight latching in the movement of the vane. It is deemed acceptable.



Figure 3.9: Magnetic sensor - final product

### 3.4 Capacitive Sensor

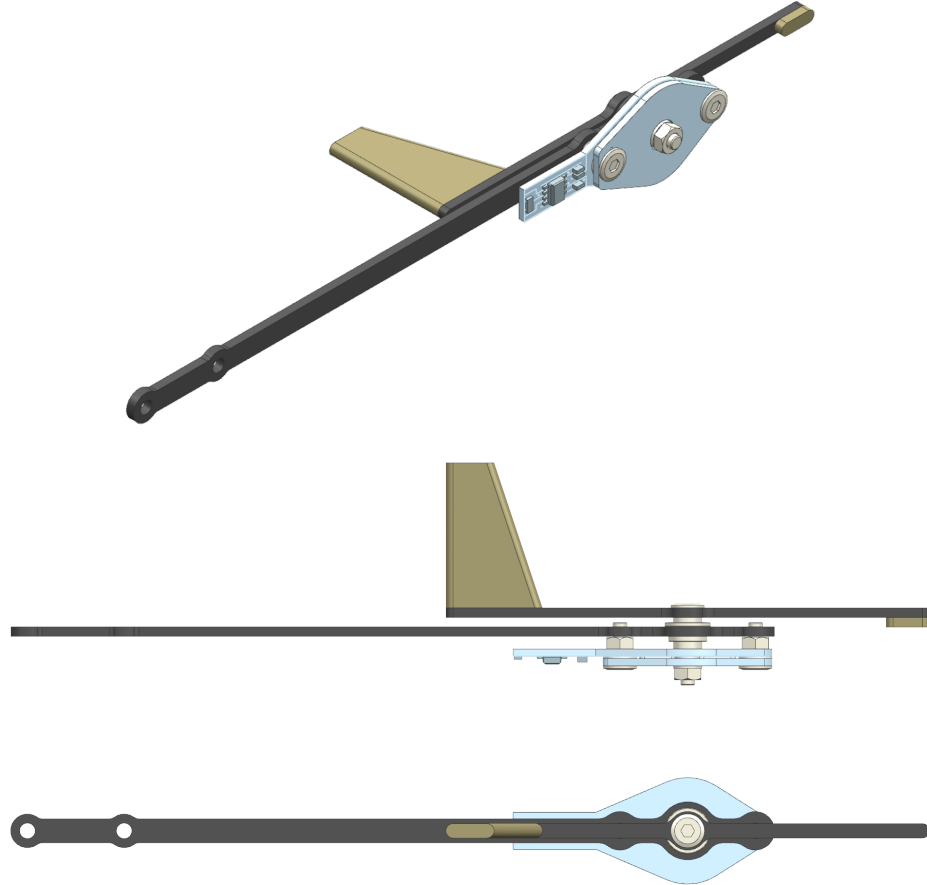


Figure 3.10: Capacitive sensor - CAD

The capacitive sensor is based on a capacitive rotary encoder. Such an encoder consists most commonly of a plate capacitor that can change its core permittivity  $\epsilon$ , plate area  $A$  or gap width  $d$  based on the axis angle creating a variable capacitor  $C = \epsilon A/d$ .

The variable capacitor in this case is realised with two plates that are fixed to the support arm and a core that rotates with the vane and changes the permittivity of the capacitor. Other solutions that vary the plate distance were rejected because of rigidity concerns and solutions that vary capacitor area were rejected because of concerns that the wire necessary to connect the moving and the stationary plate would introduce substantial friction.

Three ways to transduce the capacitance value into a form of information that is usable to the Pixhawk were found:

1. The capacitor is charged through a resistor with constant voltage. The time it takes for the capacitor to reach a threshold voltage is a measure of its capacitance according to  $V_{cap}(t) = V_{sup}(1 - e^{-t/RC})$ . To reach a voltage

of  $V_{cap} = 2/3V_{sup}$  it would take  $t_{thresh} = -\ln(1/3)RC$ . Since the maximum available resistor size lies in the  $M\Omega$  range and the capacitance is expected to be in the  $pF$  range a threshold time in the  $\mu s$  range would result. This time frame is too small to be able to detect changes in  $t_{thresh}$ .

2. A known high frequency AC signal is applied to a capacitive voltage divider where one capacitor is variable and the other is fixed. The voltage amplitude over the variable capacitance is then a measure for its capacitance. This approach is difficult as the sine wave generator circuit and the demodulation (envelope detector) circuit necessary for operation can be quite complex.
3. The easiest way to precisely measure the capacitance of a capacitor is by using a 555 timer IC in astable operation. The 555 timer continuously charges and discharges the capacitor through a resistor. While it charges, it outputs a high signal and while it discharges, it outputs a low signal. For this reason, the frequency of the output signal can be linked to the capacitance. This approach is used for all iterations of the capacitive encoder.

Figure 3.11 shows a sketch of all the components of the encoder assembly and the circuit that was used in the final iterations together with the formula that link the output frequency with the capacitance and axis angle. A derivation of the 555 timer relation and its working principle is omitted for brevity's sake. In the sketch the following symbols are used:  $d_i$  isolation gap width,  $d_c$  core width,  $A$  capacitor area ( $A = \pi D^2/2$ ),  $\epsilon_c(\alpha)$  permittivity of core as function of axis angle,  $\epsilon_c$  maximum permittivity of core,  $R$  charging resistor,  $C_1(\alpha)$  variable capacitor,  $C_2$  offset capacitor,  $C_3$  control capacitor,  $C_4$  input filtering capacitor.

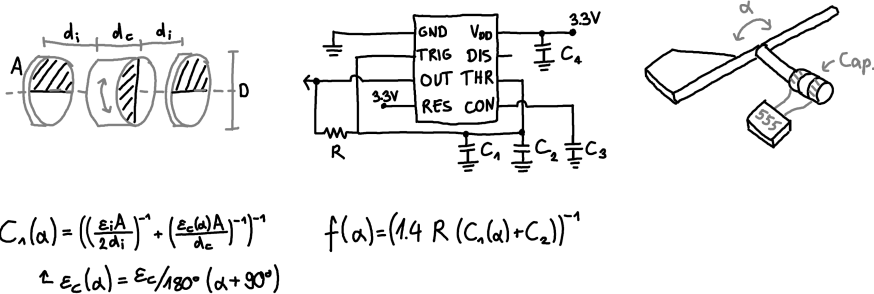


Figure 3.11: Capacitive sensor - principle

For this encoder it is hard to determine the requirements for the different components since there is a lot of uncertainty on the realisable clearances and material characteristics in the variable capacitor, and most other components depend on that. The following combination of component used in the final version of this sensor was found mostly through trial and error: The core is made of  $d_c = 0.5mm$  thin copper sheet with diameter  $D = 20mm$ . The insulation layer consists of a  $d_i = 0.06mm$  gap of half transparent tape and half air. The two capacitor plates are made of a copper-clad board. The charging resistor is a SMD thin film resistor with  $R = 1M\Omega$ .  $C_2 - 4$  are ceramic SMD capacitors with  $C_2 = 5pF$ ,  $C_3 = C_4 = 100pF$ . The 555 timer used is the “Maxim ICM7555”. This set-up results in a theoretical variable cap range of  $C_{1 min} \approx 2pF$ ,  $C_{1 max} \approx 16pF$  that in turn led to a theoretical output frequency range of  $f_{max} \approx 33kHz$ ,  $f_{min} \approx 21kHz$ . For the desired resolution of at least  $1^\circ$  to be achieved, this means a sampling rate of at most 66Hz.

Before the first working iteration there were a lot of failed iterations with various combinations of components. This type of encoder seems to be the hardest to get working reliably with the available means. A selection of used components and the reasons why they did not work is listed below.



Figure 3.12: Capacitive sensor - circuit iterations



Figure 3.13: Capacitive sensor - capacitor core iterations

- Core material:

- Paper: The permittivity is too low ( $\epsilon_r \approx 4$ ) to result in a useful capacitance range. It does have the advantage that no insulation layer is necessary.
- Viscose fabric: According to [14] viscose has a permittivity of  $\epsilon_r \approx 35$ . An experiment put this number around that of paper. It is assumed that the document is referring to viscose pulp and not viscose fabric.
- Glycerol-impregnated paper/viscose: Glycerol is a fluid with a permittivity of  $\epsilon_r \approx 40$  and very low vapour pressure (non-volatile). Its disadvantage is that it is slightly conductive and thus requires an insulation layer. No such layer could be produced as the glycerol kept seeping around the insulation after a couple of days.
- Aluminium: An aluminium core is conductive and can be approximated as  $\epsilon_r \approx \infty$ . This material also requires an insulation layer as it would short-out the capacitor if it touched both plates. Milling of a  $d_c = 0.5mm$  aluminium sheet kept resulting in a warped surface and chatter. This was possibly due to residues of the oxide layer, internal stresses or bad feed and cutting speed.
- Copper: Copper works by the same principle as aluminium. Compared to aluminium it is much easier to work with. It is the material of choice for the final iteration.

- Insulation:

- No insulator: Depending on the core material no insulation layer is necessary.
- Conformal coating: Conformal coating is a thin polymeric film that is used to protect PCBs against moisture, dust etc. The coating is sprayed on. It is presumed to be the thinnest insulation layer that was tried. It did not work reliably as it is easy to rub away and is hard to apply uniformly.
- Teflon tape: Teflon tape is used to seal threads. It is very slippery and thin. It was glued onto the cap plates with instant glue to try and reduce friction and insulate. It did not work as the Teflon tape is too prone to ripping.
- Electrical tape: This is a type of tape used to insulate electrical wires. It is very resistant, but also thick  $d = 0.12mm$  reducing the performance of the encoder.

- clear tape: Is the same as the electrical tape, only less resistant and thinner ( $d = 0.03mm$ ). This insulation was used in the final iteration.
- 555 Timer IC:
  - NA555: This requires a voltage divider for its output as the supply voltage is 5V. This has led to problems if the resistors are of the metal film type. If the resistors are too small, the timer is overloaded and if they are too big, the parasitic inductance of the resistors ruins the signal. Later iterations used thin film SMD resistors to avoid this problem.
  - TLC556: This timer uses CMOS technology that reduces current spikes and increases frequency stability for small capacitances. This particular model consists of two timers in one package allowing it to measure the capacitance on both sides of the cap plate. This can be useful when the core is not conductive to decrease noise by combining both readings. It is not used since all non-conductive cores failed to work.
  - ICM7555: Also a CMOS timer, but with even lower power draw. Used for the final iteration.
- Notes on passive components:
  - $C_2$ : The offset capacitor is necessary to offset the variable capacitor  $C_1$  by a fixed amount as the sensitivity (Hz/pF) of the 555 timer decreases with lower capacitances.
  - $C_3$ : The control capacitor is used to filter the reference voltage of an internal comparator. If it is missing, noise in the output frequency increases.
  - $C_4$ : If the input filtering capacitor is not present (especially for NA555), the noise in the output frequency increases.

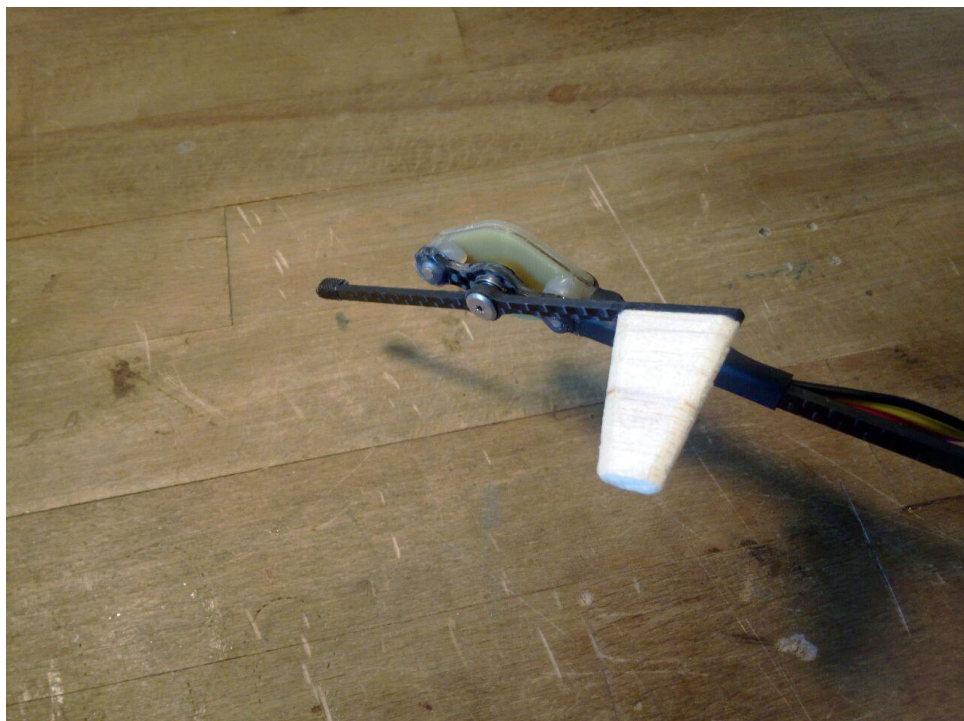


Figure 3.14: Capacitive sensor - final product

### 3.5 Positional Calibration Set-up

The positional calibration set-up is used to map the output values of the sensors to axis angles in a static environment. The reasons why this and the following wind-tunnel calibration set-up are needed, are described in chapter 4. The requirements are that the axis angle be positionable at a certain angle with an accuracy of  $\pm 2^\circ$  by hand. To accomplish this, a 16mm-thick MDF plate is used as base material. This plate is cut to shape in such a way as to precisely position a sensor by its mounting holes and support arm. A big hole is added to allow the vane to rotate. An angle scale is printed on paper and glued on to allow the tip of the vane to be positioned at certain angles. The angle scale has a spacing of  $5^\circ$  resulting in a nominal accuracy of  $\pm 2.5^\circ$  for positioning by hand. In reality much higher accuracy can be reached, but is hard to quantify.

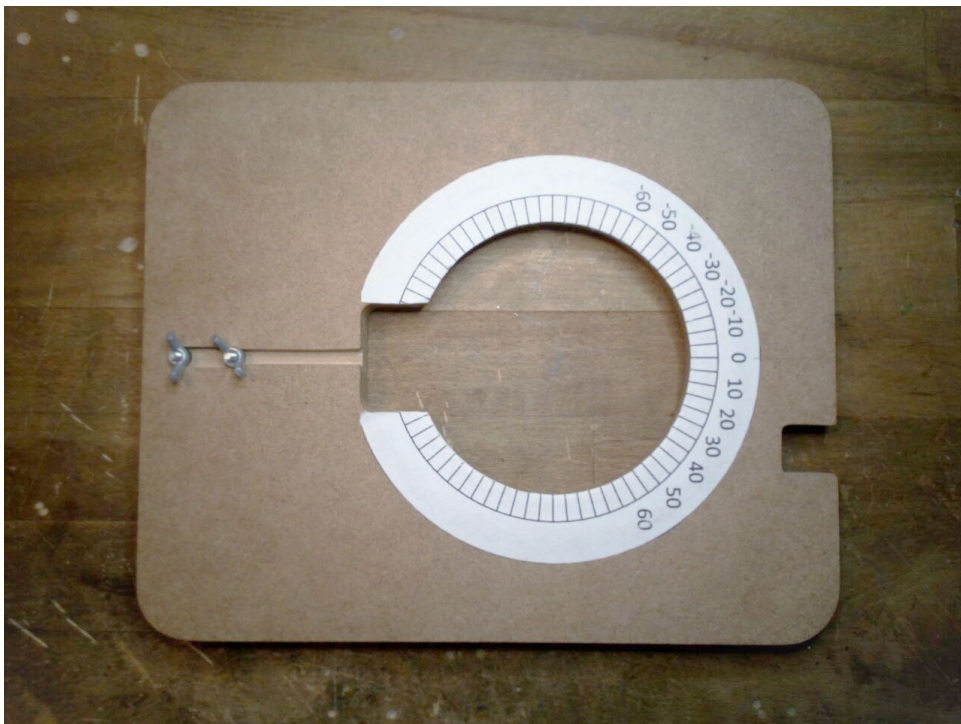


Figure 3.15: Positional calibration set-up

### 3.6 Wind-tunnel Measurement Set-up

The wind-tunnel measurement set-up is used to map the output values of the sensors to the angle of attack (which is not necessarily equal to the axis angle in a static environment). This system comprises a wind-tunnel and a motorised arm to which the AOA sensor is fixed. By moving the arm, a certain angle of attack can be set and the reaction of the sensor measured.

The only available wind-tunnel is the one provided by the Physics Department of ETH. It has an output diameter of 100mm and a airspeed range of 9m/s – 20m/s (set by a variable autotransformer, measured by a Pitot tube). It is regarded as adequate as it matches the airspeed range of the RC plane and is big enough to fit the AOA sensor.



Figure 3.16: Wind-tunnel

The motorised arm has to be able to track given input signals precisely ( $\pm 0.1^\circ$ ). It also has to have a range of min.  $\pm 45^\circ$  and a speed of at least  $60\text{rpm}$ . The arm position and AOA sensor output have to be logged with a sampling rate of at least  $100\text{Hz}$ . Most importantly, it has to be compatible in size and shape with the wind-tunnel.

Two versions of this motorised arm were made. The first and failed version is included here as it contains valuable learnings. The second version is the one that is used for all wind-tunnel logs in chapter 4.

The first version is based on the standard size servo FS5106B. Its specifications are torque=0.6Nm, range= $180^\circ$ , weight=40g, gearbox=plastic. Unlike most servos, it possesses an analog feedback output which is internally connected to a potentiometer that is internally used as feedback to control its position. In this application the analog feedback is used to determine the position of the arm as servos typically do not track their reference angle very well. This trick is used so that even if the input to the servo is not tracked well, its output is known (=AOA sensor input) and the behaviour of the sensor can be analysed.

The supporting structure of the motorised arm is mainly made of 6mm-thick MDF with aluminium tubes and threaded M3 rods to connect it to the AOA sensor. This construction is not very stiff. Especially the plastic arm-to-servo connection and the two tubes introduce a lot of flex even under very minor loads. Additionally, the gears of the servo allow for  $6^\circ$  of play making precise positioning nearly impossible.



Figure 3.17: Motorised arm - first version

The servo itself is controlled by an Arduino Due microcontroller that outputs a 50Hz PWM signal containing the requested servo angle and that reads the analog feedback voltage. It was observed that the feedback voltage spikes after every PWM pulse for a duration proportional to the load on the servo. It is assumed that this is due to an induced voltage from EMI caused by the servo motor powering up after every pulse for a time proportional to its angle error. This circumstance necessitates the feedback voltage measurement to be only taken on the rising edge of the PWM signal resulting in a 50Hz sampling rate.

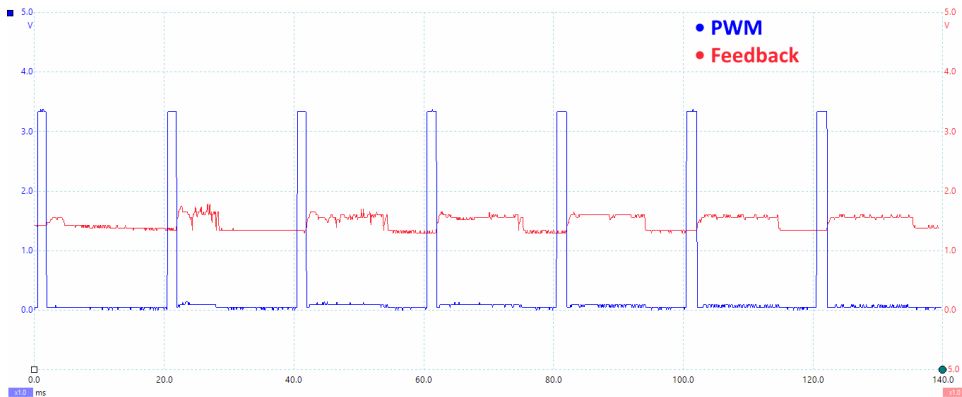


Figure 3.18: Servo PWM and analog feedback

Both, the stiffness and the sampling rate problem make the first version obviously unfit for the job as it does not conform to the requirements. The second version solves these problems.

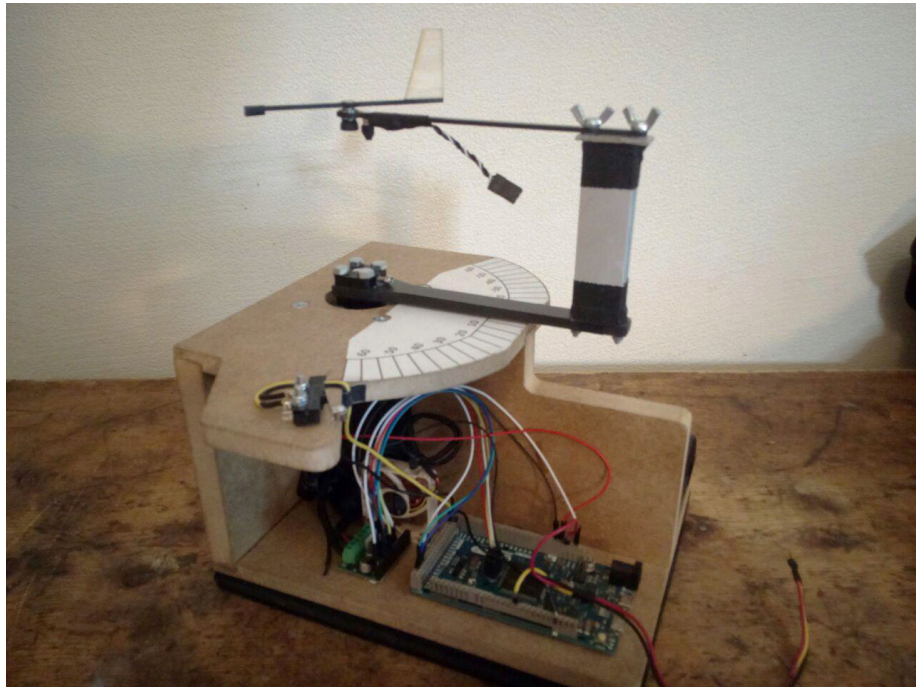


Figure 3.19: Motorised arm - final version

The stiffness problem is solved by using the following structural components: A 5mm-thick CFRP plate is used for the arm. The connection to the AOA sensor is realised through a 14x22x2mm H-beam that is clamped together by two M3 threaded rods. The arm is fixed to the motor shaft by two mounting hubs with four screws fixing it to the arm and two screws locating to the flat spot on the D-shaft of the motor. The entire base is made of 16mm-thick MDF plates connected with glued rabbet and dado joints. The resulting structure is extremely stiff and nearly no flex can be observed.

The servo motor is replaced by a NEMA 23 high torque stepper motor. It possesses substantially more torque (2.4Nm) and is able to position itself much more precisely than the servo. Since this model only has 200 steps per revolution ( $1.8^\circ$  step angle) a stepper driver with micro-stepping capabilities is installed. By sending controlled currents through each coil, the micro-stepping technology is able to position the shaft at angles between two step angles. The stepper driver used, is “AMIS-30543”. It allows for coil currents up to 3A (with heat sink and forced air-flow) and up to 1/128 stepping, resulting in  $200 * 128 = 25600$  steps per revolution ( $0.01^\circ$  step angle). Power is delivered through a power brick rated for 30V 0.7A DC and step orders are given by an Arduino Due microcontroller that also logs the sensor data.

Stepper motors do not possess any position feedback. Rotary encoders for the desired resolution are too expensive, so a homing switch is installed. At power-up the arm will rotate until it triggers the switch, at which point it will know where it is positioned. The position after that moment is determined by counting the steps taken in each direction and summing them up. To detect if there is a significant load on the stepper, which would make the arm lag behind its target position, the back-EMF voltage is continuously read through the stepper controller. Additionally, the homing cycle is repeated at the end of each measurement cycle to determine if the home position is still in the same place based on the performed steps.

The code running on the Arduino Due microcontroller consists of a loop that for each iteration determines if a step is necessary to follow some required signal. The requirement of being able to rotate the stepper with at least  $60\text{rpm}$ , poses significant challenges as it means that each loop iteration must be completed in  $40\mu\text{s}$  (non optimised code required  $200\mu\text{s}$ ). This speed-up is reached with various tricks:

- A significant bottleneck is the serial connection to the PC for logging. If standard ASCII encoding is used, each data packet is  $\approx 23\text{byte}$  in size, taking  $\approx 80\mu\text{s}$  to encode. By using COBS encoding, the packet size can be reduced to  $9\text{byte}$  and the encode time to  $5\mu\text{s}$ . COBS is a byte stuffing process that encodes the binary data packet in such a way as not to use the  $0x00$  byte. This allows for that byte to be used as packet delimiter and to detect dropped bytes.
- Only one byte is sent to the PC on every loop iteration to minimise its impact. If it is not done, spikes in loop time would result, thus missing steps.
- The baud rate (speed in bits per sec) of the serial connection is raised to the maximum of 250000 for the Arduino due, after which data transfers would become unreliable.
- No floating point or 64bit integer variables are used throughout the program as calculations with them are significantly slower than those of 8-32bit integer variables on the Arduino due platform (Atmel SAM3X8E 32-bit ARM core). When floating points are necessary, integers are used instead that are multiplied by some power of ten (e.g.  $1.23456 \rightarrow 1.23456 \cdot 1000 \approx 1234$ )
- Division and modulo operations are avoided as much as possible as they are significantly slower than multiplication, addition and subtraction operations.
- All “waiting times” (like the minimum time that the step signal for the stepper controller needs to stay high enough to be detected (min.  $3\mu\text{s}$ )) are spent calculating and no inactive time is scheduled.
- Complex functions like the sine function or the logistics function (used for chirp and step signals) are pre-calculated and saved in look-up tables where the function value is determined through interpolation at runtime.
- To further decrease the load on the microcontroller, the required arm positions are calculated 1ms in advance and the position linearly interpolated to it during that time.

All these measures to optimise the code have led to an overshooting of the requirements allowing for  $120\text{rpm}$  at  $500\text{Hz}$  sampling rate.

The resistive and magnetic AOA sensors are read by a 12-bit ADC on every loop iteration ( $\approx 50\text{kHz}$ ) and the average between two log packets are sent to the PC ( $= 500\text{Hz}$ ). The capacitive AOA sensor counts the number of pulses between two log packets with a rising edge interrupt and converts that value into a frequency number.

As can be seen in Figure 3.19, the AOA sensors are mounted perpendicularly to their operating orientation. This nullifies the effect that gravity might have on them. Since these AOA sensors will be mounted on small-scale aircraft that typically fly over a wide range of orientation, it is possible that gravity will add varying disturbances to the sensor readings. This disturbance is assumed to be low since the vanes are mass-balanced. This is ignored in the analysis.

# Chapter 4

## Analysis

The last part of this thesis, after having designed and built three different angle of attack sensors, consists of the analysis of these sensors. The analysis is done by first introducing and discussing different test cases with different set-ups. These tests comprise static tests where only the steady-state response to certain inputs is analysed and dynamic tests where the time-dependent response is analysed. Their objective is to quantify different performance metrics and through them compare the three sensors to each other.

### 4.1 Test Cases

#### 4.1.1 Positional Calibration

The positional calibration uses the plate described in section 3.5. It is intended to generate a rough mapping between sensor output and vane angle. The vane angle here is not necessarily equal to the angle of attack with the same sensor reading, as it is not given that the vane stabilises parallel to the wind (due to aerodynamic effects from the support arm).

This positional calibration is used to get a quick impression on the range (*Does the sensor provide readings over all angles?*), noise (*Are the readings always the same for the same angle?*) and hysteresis (*Is there a difference in readings while going up respectively down the scale?*). The calibration process is designed to be quick and is used throughout the building process to assess progress. For this reason, the positional calibration set-up is only required to have a positioning precision of  $\pm 2^\circ$ . For the final analysis these measurements are compared with those of a calibration in the wind tunnel (subsections "*Wind-tunnel Calibration*") to determine if there is a significant difference between vane angle and angle of attack.

The test is executed by starting the sensor at  $-60^\circ$ , moving it up at  $5^\circ$  increments to  $+60^\circ$ , moving it back down at  $5^\circ$  increments to  $-60^\circ$  and repeating the sequence three times, totalling 6 measurements per angle and 150 total measurements. The measurements themselves are taken after the sensor output has stabilised and are calculated by averaging the sensor outputs over time so that the measurement has negligible noise.

### 4.1.2 Wind-tunnel Tests

All the wind-tunnel tests use the motorised arm described in section 3.6 to measure the response of the angle of attack sensors to different signals in a wind-tunnel. Based on the capabilities of the wind-tunnel it was decided to perform all the tests at airspeeds of 10m/s, 15m/s and 20m/s to try and detect dependencies on the airspeed in the sensor model and calibration. It is expected that the most relevant dynamics will happen below 10Hz. For this reason, it is required that the motorised arm sample with at least 100Hz (500Hz is reached). Based on the 1° resolution requirement for the sensors, it is required that the motorised arm be able to position itself with a precision of at least  $\pm 0.1^\circ$  so that the compliance can be verified (The motorised arm accomplishes this).

#### Ramp Response

The objective of the ramp response measurement is to create a continuous calibration curve that links the actual angle of attack to the sensor output in a quasi-steady-state.

To accomplish this objective, the ramp function consists of two linear ramps from  $-45^\circ$  to  $+45^\circ$  to  $-45^\circ$ . The time it takes to perform one ramp is chosen to be 30s. By picking such a long time, any dynamic effects can be effectively ruled out (definitive confirmation can follow from the step response). The response of the sensors to the ramp signal can then be used to determine the constants in a generalised form of the AOA  $\leftrightarrow$  sensor output relation. This is accomplished by picking the constants in such a way that the average error between the calibration curve and all measurement points is minimised. The process is called non-linear least square fitting and the resulting error is the root-mean-square error (RMSE).

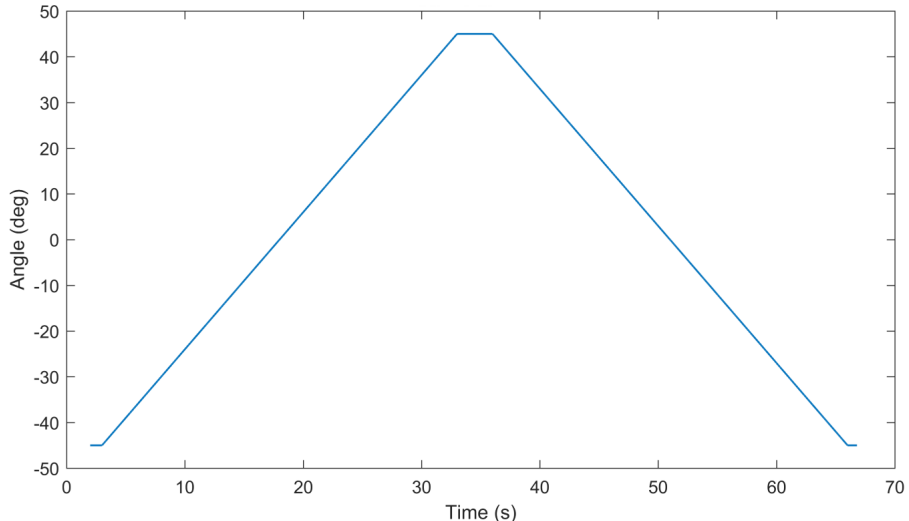


Figure 4.1: Ramp signal

### Step Response

The step response measurement has two purposes. On one hand it is used to perform a linear time domain system identification of the sensor. By developing such a model of the sensor, deductions about its performance can be made (e.g. sensor delays, possible frequency range, ...). This is done by starting from different reference angles in order to be able to determine if the sensor model can be assumed to be linear. On the other hand, it is used to determine the steady-state response at various angles as after every step the position is held until after the vane has stabilised.

The step function consists of 12 steps of  $15^\circ$  going from  $-45^\circ$  to  $+45^\circ$  and back to  $-45^\circ$ . Each step has a width of 100ms inside of which it is treated as a sigmoid function (logistic curve) to reduce the probability of the stepper of the motorised arm skipping a step. After a step the vane is given 2s to stabilise on the new equilibrium (presumably longer than the time to reach steady-state).

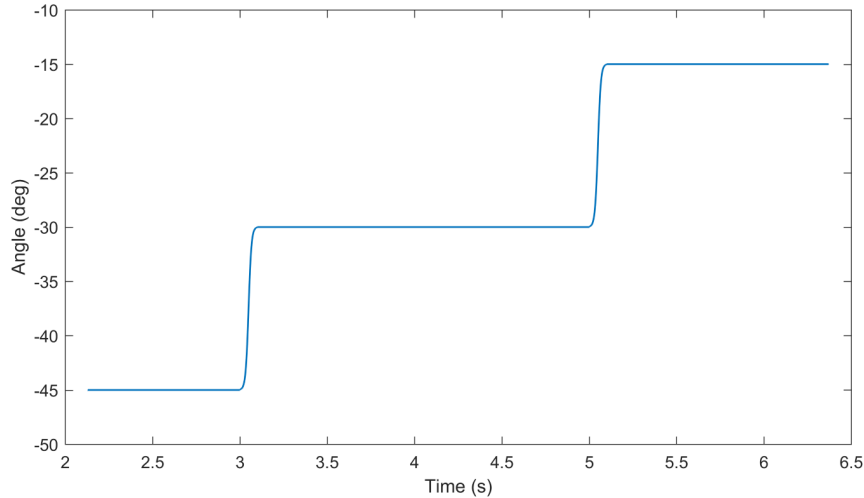


Figure 4.2: Step signal (first two steps)

### Chirp Response

The chirp response measurement is supplementary to the step response in that it is used for frequency domain system identification instead of a time domain identification. The system identification in the frequency domain has the same objectives as the one in the time domain and should give similar results.

The used Chirp signals are defined by a sine wave that changes its frequency from a start to an end-value linearly over time while keeping the amplitude constant. Concretely, the amplitude is  $A = \pm 15^\circ$ , the start frequency is  $f_{start} = 0.1\text{Hz}$ , the end frequency is  $f_{end} = 3\text{Hz}$  and the chirp duration is  $T = 30\text{s}$ . This chirp manoeuvre is performed around the angles  $-30^\circ$   $-15^\circ$   $0^\circ$   $15^\circ$   $30^\circ$ . These values are picked based on the capabilities of the motorised arm and time constraints for using the wind-tunnel.

Data from this measurement is largely unused in the analysis as a chirp response can only reliably provide information about the system inside its chirp frequency. Unfortunately, most dynamics will be shown to be happening above the end frequency of  $f_{end} = 3\text{Hz}$  making the chirp response useless for system identification.

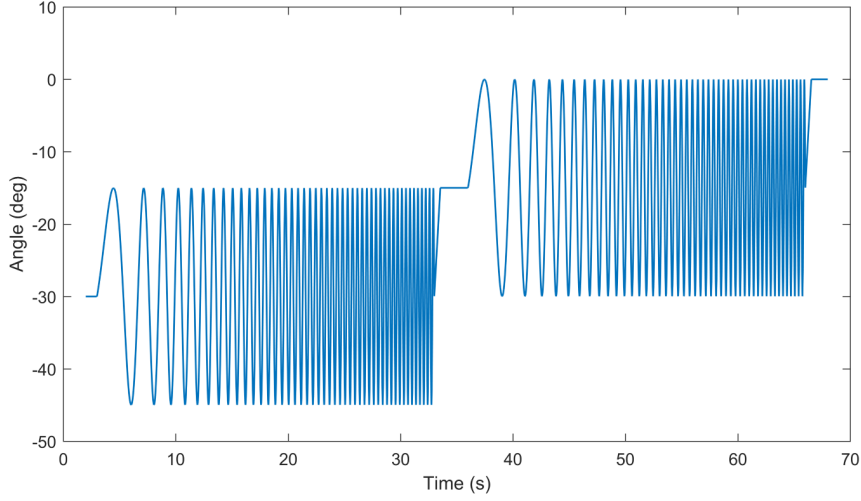


Figure 4.3: Chirp signal (first two chirps at  $-30^\circ$  and  $-15^\circ$ )

### Random Response

The random response measurement is the last that is taken in the wind-tunnel with the motorised arm. It is used to test the validity of the time and frequency domain models of the angle of attack sensors. This is done by comparing the actual AOA sensor response with the one predicted by the two models.

The signal consists of a semi randomly chosen sequence of 321 steps. The steps range from  $5^\circ$  to  $20^\circ$  and the intervals between steps range from 100ms to 1000ms (presumably less than it takes to reach steady-state). The direction of the steps follows a pattern of up→down→up until  $45^\circ$  is reached, then a pattern of down→up→down until  $-45^\circ$  is reached. This is repeated for six passes.

The random response remains unused in the analysis as no sensors perform well enough to allow a modelling of their behaviour as the following data will show.

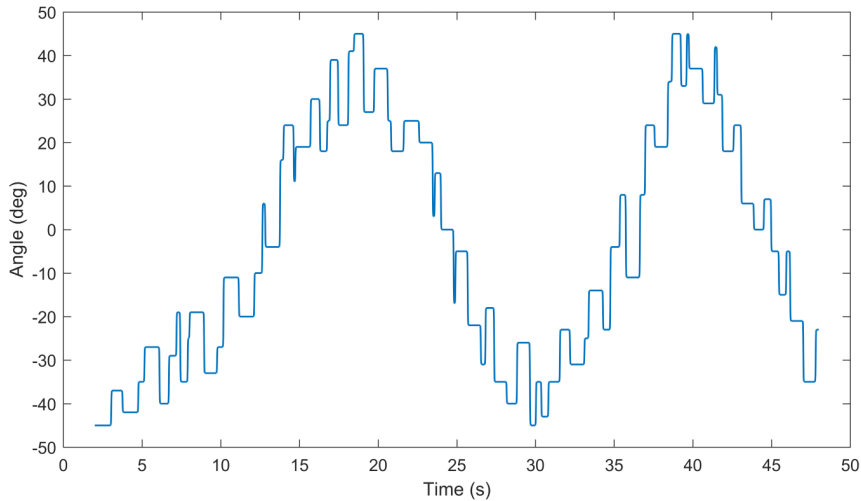


Figure 4.4: Random signal (two of the six passes)

## 4.2 Resistive Sensor

### Positional Calibration

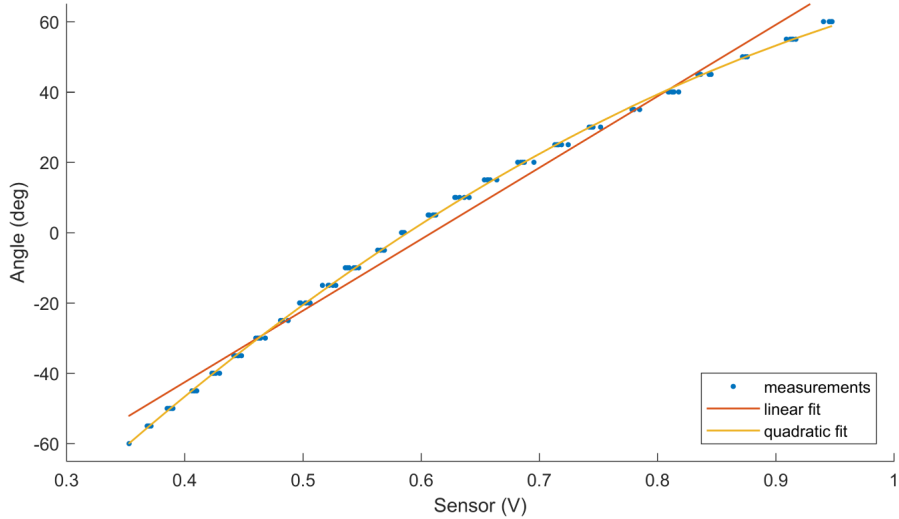


Figure 4.5: Resistive sensor - positional calibration

Figure 4.5 shows the results of the positional calibration of the resistive sensor. Blue dots represent the measurement points. At a first glance no hysteresis can be observed and there appears to be a strong correlation between the angle  $\alpha$  and the sensor output  $v$  in volt. According to the physical principles described in section 3.2 a linear correlation is expected. A least-square fit results in function 4.1 (orange line) with a root-mean-square error (RMSE) of  $4.1^\circ$ . Apparently, the potentiometer is not perfectly linear. This is presumably caused by imperfections in the resistive strip that makes the resistance change inconsistently over its length. By assuming a quadratic correlation, the resulting function is 4.2 (yellow line) with a root-mean-square error of  $0.8^\circ$ . Most of the RMSE is assumed to be due to the manual positioning of the vane.

$$\alpha(v)_{lin\ pos} = 203.2v - 123.8 \quad (4.1)$$

$$\alpha(v)_{quad\ pos} = -152v^2 + 397.3v - 181.2 \quad (4.2)$$

### Wind-tunnel Calibration

Figure 4.6 shows the wind-tunnel calibration of the resistive sensor. The blue line represents the rising edge of the ramp response and the light blue points represent the steady-state response after a rising step. The orange and yellow lines are the equivalents for falling ramps and steps. The black line is the positional calibration line from the above paragraph.

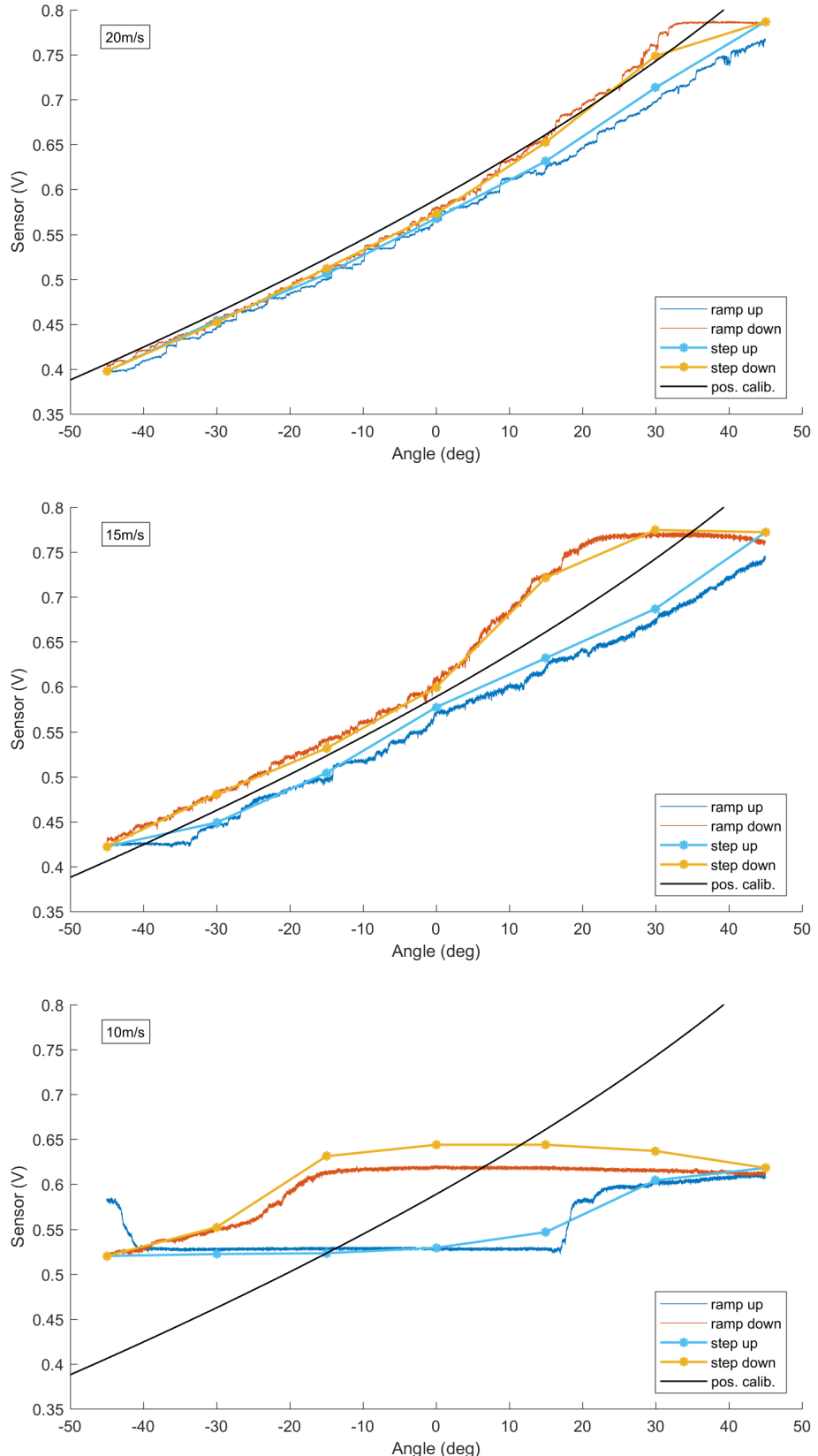


Figure 4.6: Resistive sensor - wind-tunnel calibration (20m/s, 15m/s, 10m/s)

From the plots it can be observed that hysteresis is present and increases with lowering airspeeds. This is presumably due to the increasing influence of friction as the torque acting on the vane based on the interaction of airflow and wing decreases with decreasing airspeed. It causes the vane to lag behind as more angle between vane and airflow is required to produce the torque necessary to overcome the friction of the encoder. This effect causes the vane to completely stop moving at 10m/s airspeed.

It is noticed that the hysteresis is more pronounced on the upper part of the angle range. This is presumably because this section has higher friction, as can be felt by moving the vane by hand. It is most probably due to manufacturing defects.

By observing a section of the rising ramp response at 20m/s (Figure 4.7) a stair pattern can be seen. The same pattern is visible at 15m/s and for falling ramps. The most probable explanation for this behaviour is the difference between static friction (when the vane is stationary) and sliding friction (when the vane moves) in the encoder and the bearing. Generally, the static friction is higher than the sliding friction [15]. Assuming that the vane is not moving, it will stay stationary until the pushing air overcomes the static friction (making it move). From that instant a lower sliding friction is present. This causes the vane to jump forward further than would be possible under static friction. After that the vane stops, static friction is again present and the vane has to wait until the static friction is overcome. This cycle produces a stair pattern in the movement of the vane.

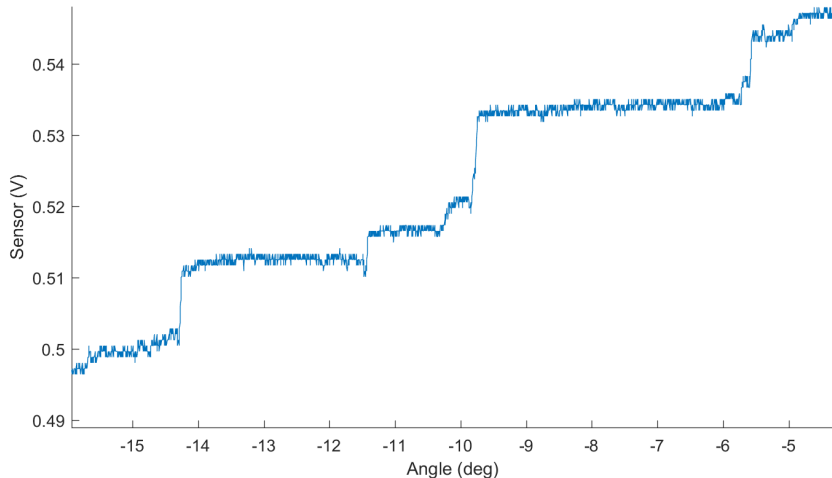


Figure 4.7: Resistive sensor - rising ramp response section (20m/s)

Because of the high hysteresis and low airspeed range, a wind-tunnel calibration curve can not be determined. The sensor is thus not usable for any real application as long as those problems are not solved.

### System Identification

The system identification of the resistive sensor was performed regardless of the problems described above. A first-order system is used to identify a time constant respectively corner frequency. Each step/chirp response is normalised separately because no calibration curve is available. This leaves the possibility open that the hysteresis skews the results.

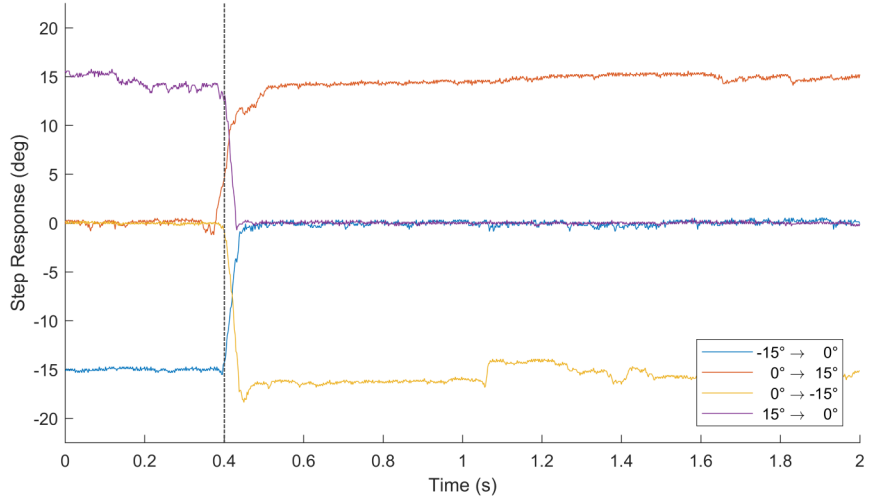


Figure 4.8: Resistive sensor - step responses at  $0^\circ$ , 20m/s

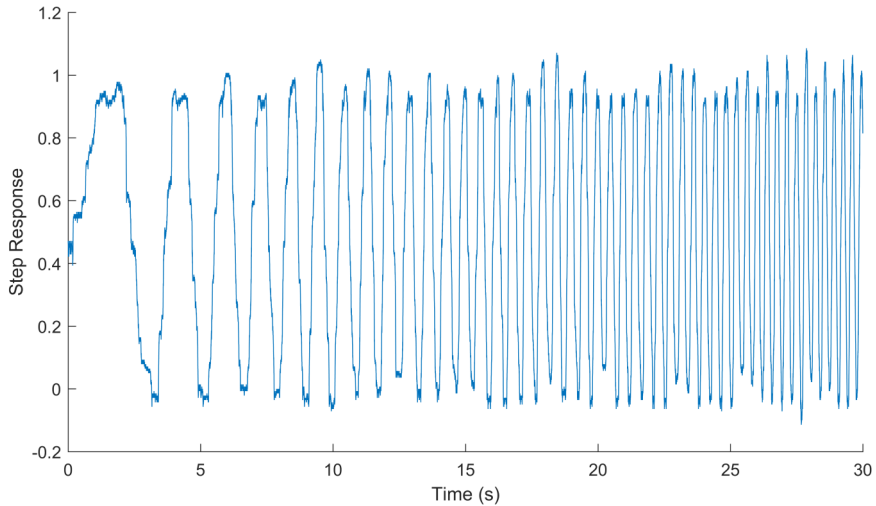


Figure 4.9: Resistive sensor - chirp responses at  $0^\circ$ , 20m/s

Table 4.1 shows the time constant of a first-order system fitted to the step responses of the sensor. The corresponding fit quality is noted in parentheses beside it. This is listed for all three airspeeds and for five reference angles.

The data shows an increase in the time constant with decreasing airspeeds and increasing reference angles. The decrease in airspeed goes so far as to make the sensor not react at all to a step signal at 10m/s. Both these observations can be explained by the same effect of friction causing hysteresis that was explained in the paragraph *Wind-tunnel Calibration*. With this information the sensor can not be assumed to be a linear system.

The chirp response can not be used to determine the corner frequency of the first-order system as it appears to be much higher than the chirp end frequency  $f_{end} = 3\text{Hz}$  over all airspeeds and all reference angles.

	-30°	-15°	0°	15°	30°
20m/s	28ms (89%)	17ms (92%)	14ms (89%)	17ms (90%)	36ms (87%)
15m/s	46ms (85%)	40ms (90%)	43ms (92%)	69ms (86%)	113ms (66%)
10m/s	-ms (0%)				

Table 4.1: Resistive sensor - time constants for different angles and airspeeds

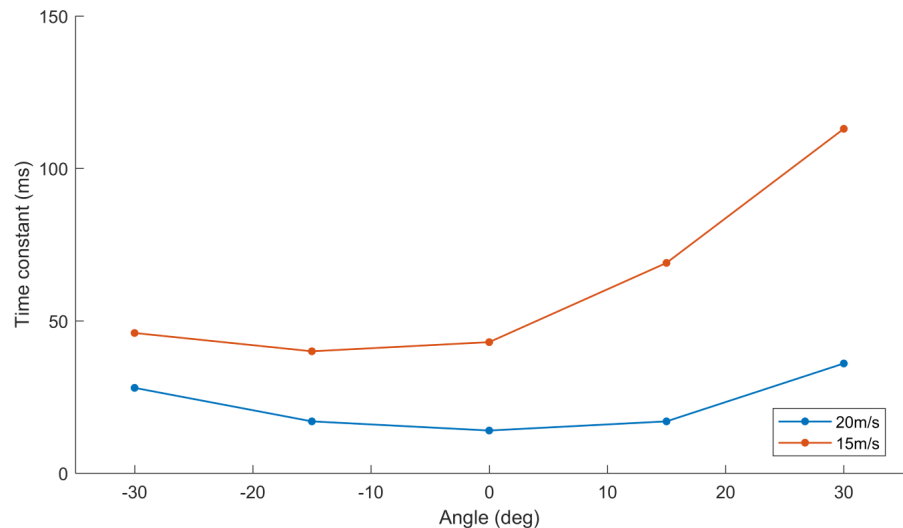


Figure 4.10: Resistive sensor - plot of table 4.1

### 4.3 Magnetic Sensor

#### Positional Calibration

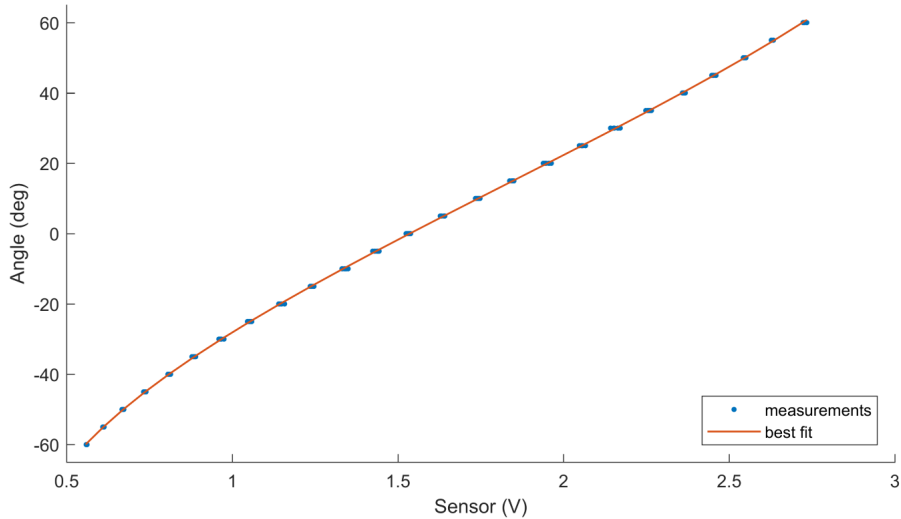


Figure 4.11: Magnetic sensor - positional calibration

Figure 4.11 shows the results of the positional calibration of the magnetic sensor. Like for the resistive sensor, the blue dots represent the measurement points. The data points appear to be even closer together than those of the resistive sensor. The formula introduced in section 3.3 states that the relation between the angle of attack  $\alpha$  and sensor output voltage  $v$  will be of the form  $\alpha(v) = \arcsin(C_1v + C_2)C_3 + C_4$ .  $C_3$  and  $C_4$  are added here, as there can be alignment errors in how the magnet is mounted. A non-linear least square fit is used to determine the constants resulting in function 4.3 (orange line). The root-mean-square error for this function is  $0.3^\circ$ . Most of this error is assumed to be due to the manual positioning of the vane.

$$\alpha(v)_{pos} = \arcsin(0.6852v - 1.2571) 69.8 + 14.4 \quad (4.3)$$

#### Wind-tunnel Calibration

Figure 4.12 shows the wind-tunnel calibration of the magnetic sensor. The blue line represents the rising edge of the ramp response and the light blue points represent the steady-state response after a rising step. The orange and yellow lines are the equivalents for falling ramps and steps. The black line is the positional calibration line from the above paragraph.

The first aspect that catches one's eye is that there does not appear to be any hysteresis. Also, the plots are very similar over all airspeeds, although they deviate from the positional calibration curve. This is presumably explained by aerodynamic effects caused by the supporting arm of the sensor. Depending on the angle of attack, the supporting arm is in a different position relative to the vane and influences the airflow differently. This influence can be modeled adequately with the linear function 4.4 resulting in a root-mean-square error of  $2.9^\circ$ .

$$\alpha_{wind} = 1.0716 \alpha_{pos} + 0.14 \quad (4.4)$$

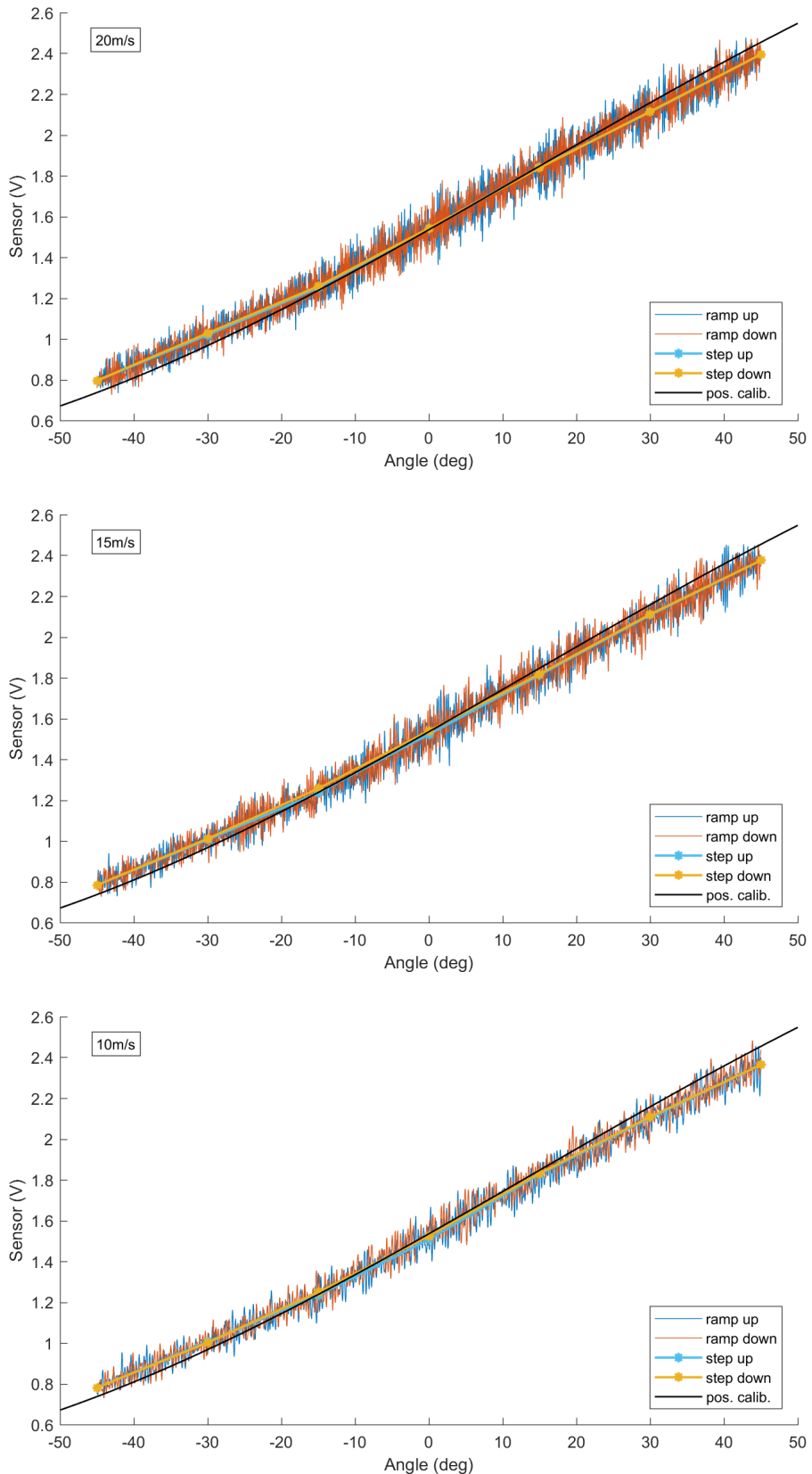


Figure 4.12: Magnetic sensor - wind-tunnel calibration (20m/s, 15m/s, 10m/s)

It was observed that the high noise on the data is caused by the vane being unstable and oscillating in the airflow. The frequency of this oscillation has been measured to be approximately 16Hz for 20m/s airspeed, 12Hz for 15m/s and 8Hz for 10m/s. Possible factors causing the oscillation are turbulence in the airflow of the wind-tunnel, turbulence caused by the tip of the vane, bad wing design and bad bearing of the rotation axis (on only one point unlike for resistive and capacitive sensors).

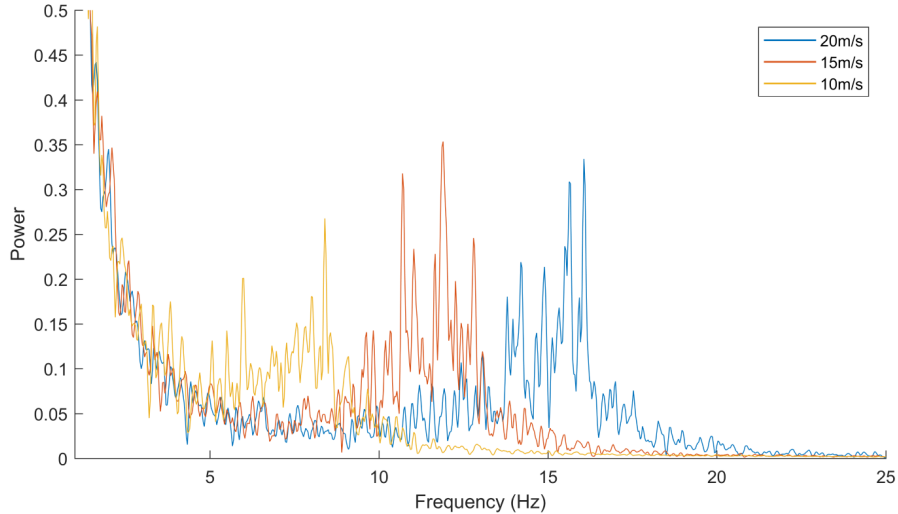


Figure 4.13: Magnetic sensor - spectral analysis of ramp response

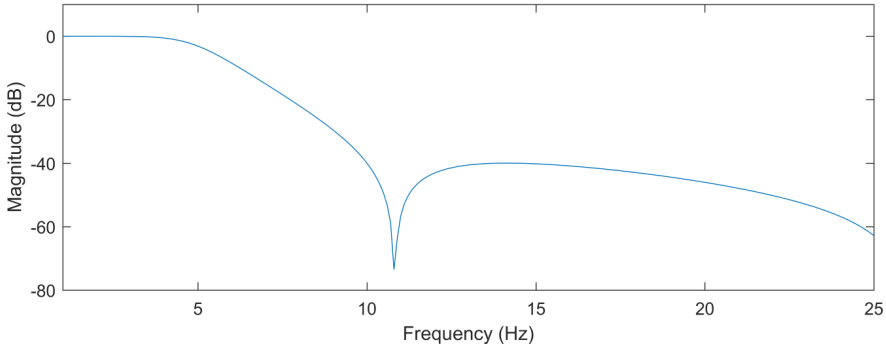


Figure 4.14: Magnetic sensor - proposed Chebyshev filter

One way to reduce the effect of this problem is to introduce a low-pass filter. A Chebyshev type II filter is proposed, as it has a good trade-off of fast roll-off at the cut-off frequency and low ripple over the pass-band. It was compared against Butterworth, Chebyshev type II and elliptic filters. The filter is chosen to be of 4<sup>th</sup> order with -40dB stop-band attenuation and 10Hz stop-band edge frequency. These parameters try to attenuate as much of the noise as possible without excessively impacting lower frequencies as can be seen in figure 4.14. Using a low-pass filter has the disadvantage that it not only filters high frequency noise, but also high frequencies that are actually part of the AOA signal. The subsequent tests will be analysed with and without the filter to show its impact on the performance.

With the proposed above and the already calculated wind-tunnel calibration function the root-mean-square error can be lowered to  $0.9^\circ$  over all airspeeds.

Since the noise frequency appears to be dependent on the airspeed one could also look into a more complex filter that takes the airspeed from a Pitot probe into account while filtering the data, thus further increasing accuracy. This was not done within the scope of this thesis.

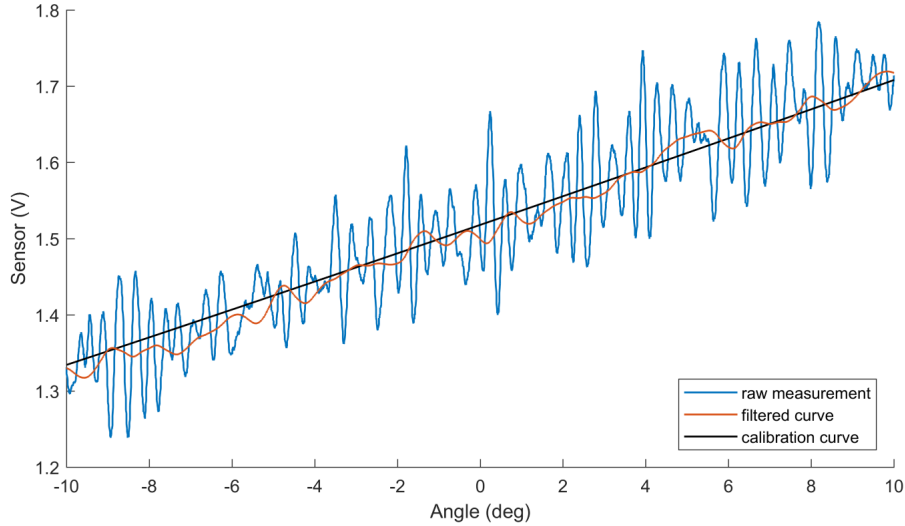


Figure 4.15: Magnetic sensor - noise on the 20m/s ramp signal

### System Identification

The system identification of the magnetic sensor was performed with and without the proposed filter. A first-order system is used to identify a time constant respectively corner frequency. Due to the high noise in the unfiltered output signal it is impossible to perform the system identification as the fit quality is between 50% and 60% over all reference angles and airspeeds.

Fitting the model on the filtered step response produces a time constant of about 162ms over all airspeeds and reference angles (with fit qualities of about 77%). This number is very close to the time constant of a first-order approximation of the filter, which is 157ms. It indicates that the sensor model must have a very low time constant.

Like for the resistive sensor, the chirp response cannot be used to determine the corner frequency of the first-order system as it appears to be much higher than the chirp end frequency  $f_{end} = 3\text{Hz}$  over all airspeeds and all reference angles.

	-30°	-15°	0°	15°	30°
20m/s	0ms (50%)	2ms (56%)	1ms (53%)	0ms (54%)	2ms (52%)
15m/s	0ms (50%)	0ms (52%)	0ms (56%)	5ms (56%)	0ms (50%)
10m/s	16ms (65%)	9ms (61%)	0ms (50%)	1ms (60%)	3ms (62%)

Table 4.2: Magnetic sensor - time constants of step response for different angles and airspeeds (without filter)

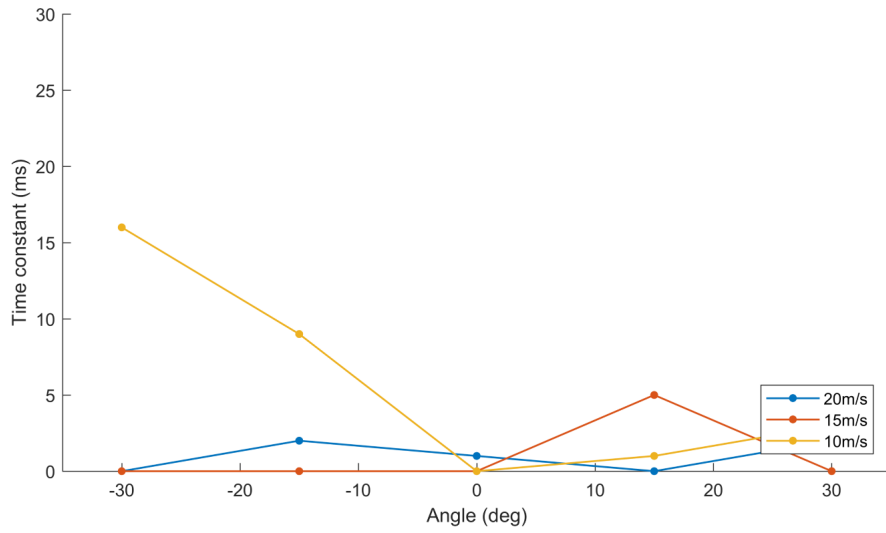


Figure 4.16: Magnetic sensor - plot of table 4.2

	-30°	-15°	0°	15°	30°
20m/s	159ms (80%)	160ms (79%)	166ms (79%)	160ms (77%)	165ms (77%)
15m/s	152ms (77%)	144ms (78%)	156ms (79%)	163ms (76%)	171ms (76%)
10m/s	179ms (75%)	179ms (77%)	173ms (77%)	158ms (77%)	149ms (75%)

Table 4.3: Magnetic sensor - time constants of step response for different angles and airspeeds (with filter)

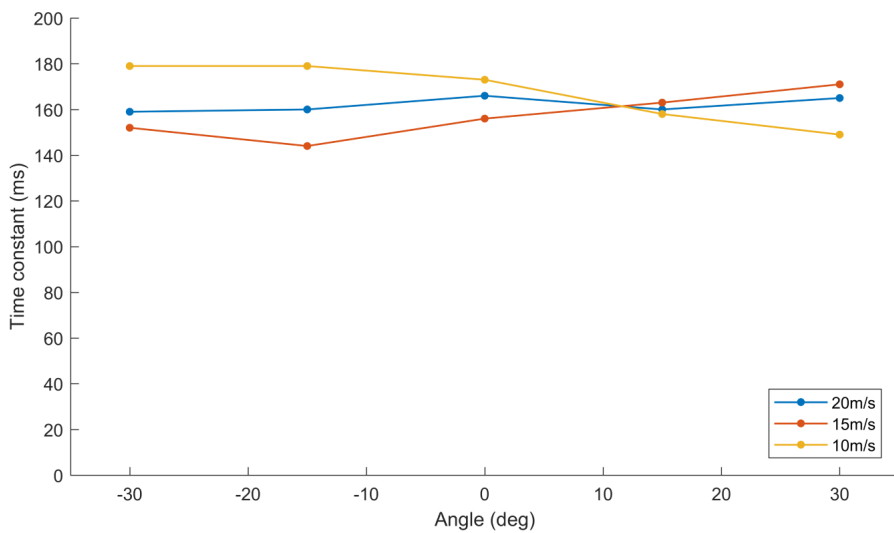
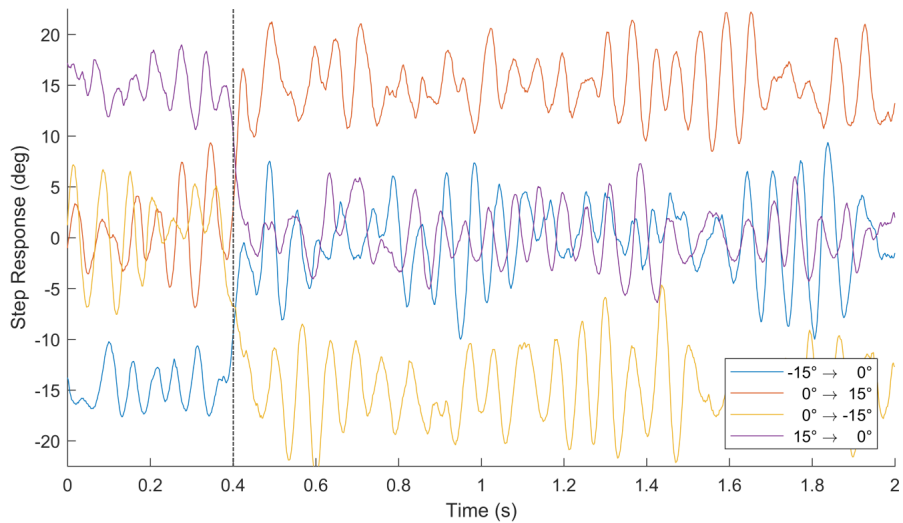
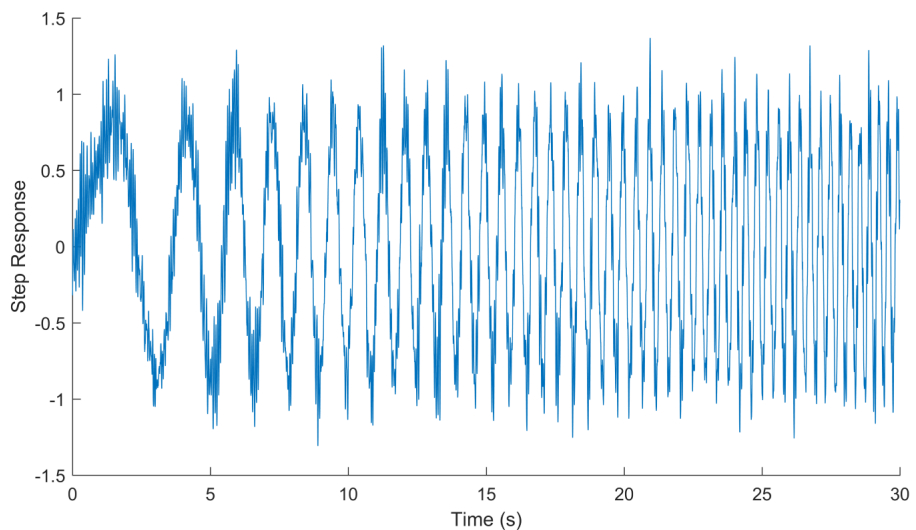


Figure 4.17: Magnetic sensor - plot of table 4.3

Figure 4.18: Magnetic sensor - step responses at  $0^\circ$ ,  $20\text{m/s}$ Figure 4.19: Magnetic sensor - chirp responses at  $0^\circ$ ,  $20\text{m/s}$

## 4.4 Capacitive Sensor

### Positional Calibration

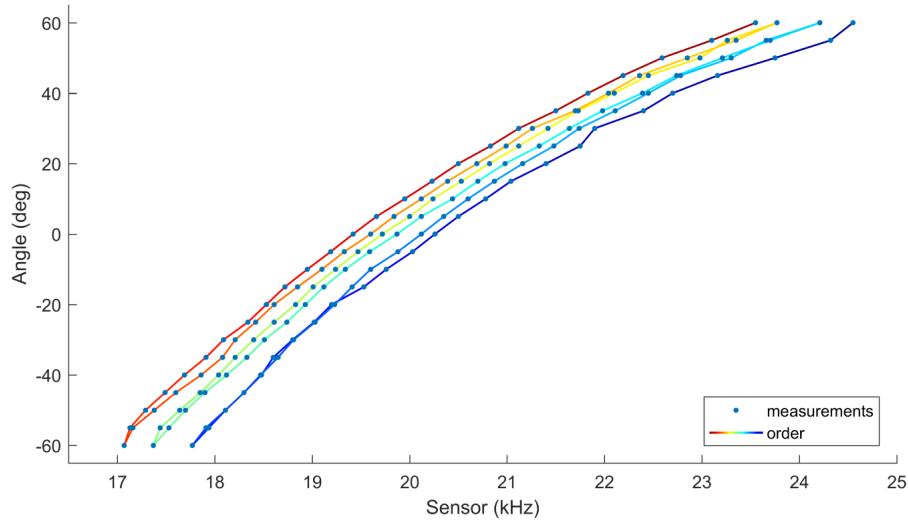


Figure 4.20: Capacitive sensor - positional calibration

Figure 4.20 shows the results of the positional calibration of the capacitive sensor. The line with the colour gradient shows the order in which the measurements were taken from the first in red via yellow and green to the last in blue. The measurements happened at approximately equal intervals during a time-frame of about 30min. The data shows a drift in the sensor output frequency of about  $28\text{Hz}/\text{min}$  (apparent increasing capacity). This drift makes a calibration impossible.

A set of experiments was created to further observe this behaviour. The positional calibration set-up (section 3.5) is used to hold the capacitive sensor fixed at  $0^\circ$  while the output frequency is logged every 30s (figure 4.21). This is done under different circumstances: Logs under the green bar are done with the sensor always powered on, while logs under the red bar are done by turning the sensor on for 1s during the measurement. Blue plots are done as described above, orange plots are done with active cooling provided by one 80mm computer fan pointing at the encoder and violet plots are done with a nearly identical backup encoder that has  $C_2 = 3\text{pF}$  and the variable capacitor  $C_2$  replaced by a  $10\text{pF}$  ceramic capacitor.

All tests were done consecutively without pauses for 24h + 8h. Hours 2 to 4 have been lost due to human error. Care was taken not to let environmental factors like temperature change over the course of the test but constancy can not be guaranteed.

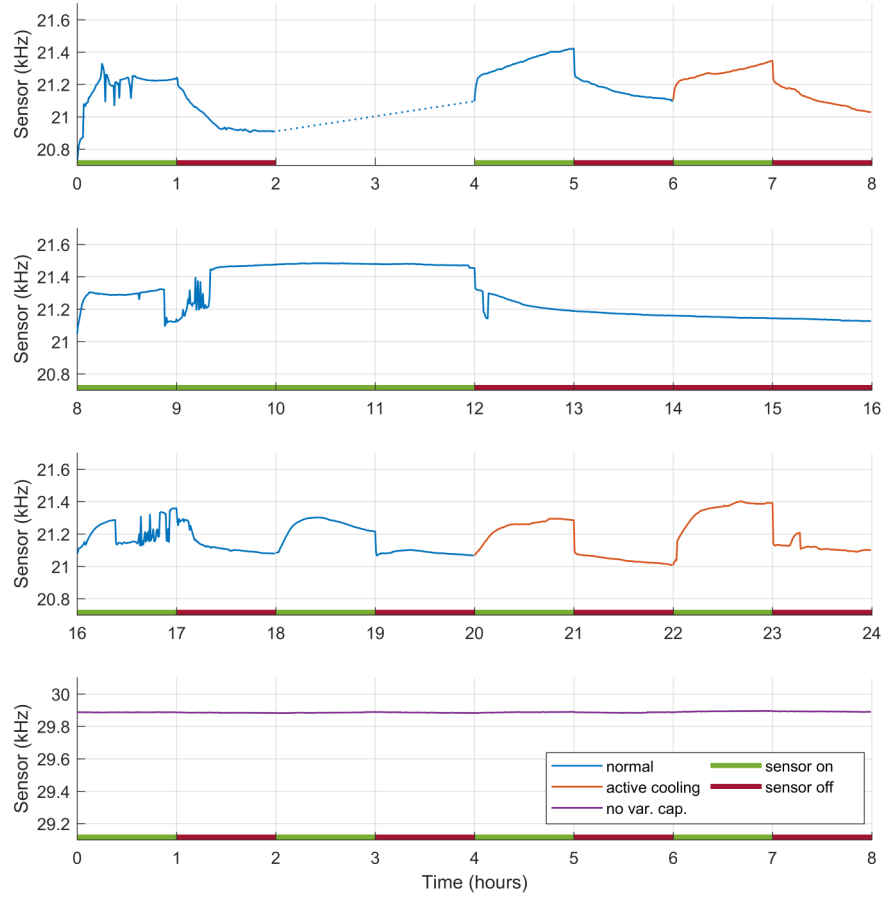


Figure 4.21: Capacitive sensor - drift experiment

It is hard to extract meaningful conclusions from the data as it does not seem very consistent. In general, the frequency drift is continuous (except at 0.5h, 9.2h and 16.8h) and in general the frequency goes up when the sensor is on and down when it is off (except at 16.6h and 19.4h). No meaningful analysis of the "turn-on" and "turn-off" curves can be made as they wildly differ from try to try. The active cooling of the encoder does not seem to affect the drift suggesting that it is not caused by heat generation. The only meaningful conclusion that can be taken is that the drift is caused by some interactions in the variable capacitor  $C_1$  as when it is replaced by a fixed capacitor, the drift stops.

No explanation for the frequency drift was found, and the pursuit of one was abandoned as it would require significant time and means that were not available at the time.

### Wind-tunnel Calibration

Figure 4.22 shows the wind-tunnel calibration of the magnetic sensor. The blue line represents the rising edge of the ramp response and the orange line represents the falling edge of the ramp response. Steady-state points from the step responses are omitted because the drift problem makes them not correlate with the ramp response. A positional calibration curve does not exist for this sensor due to the same problem.

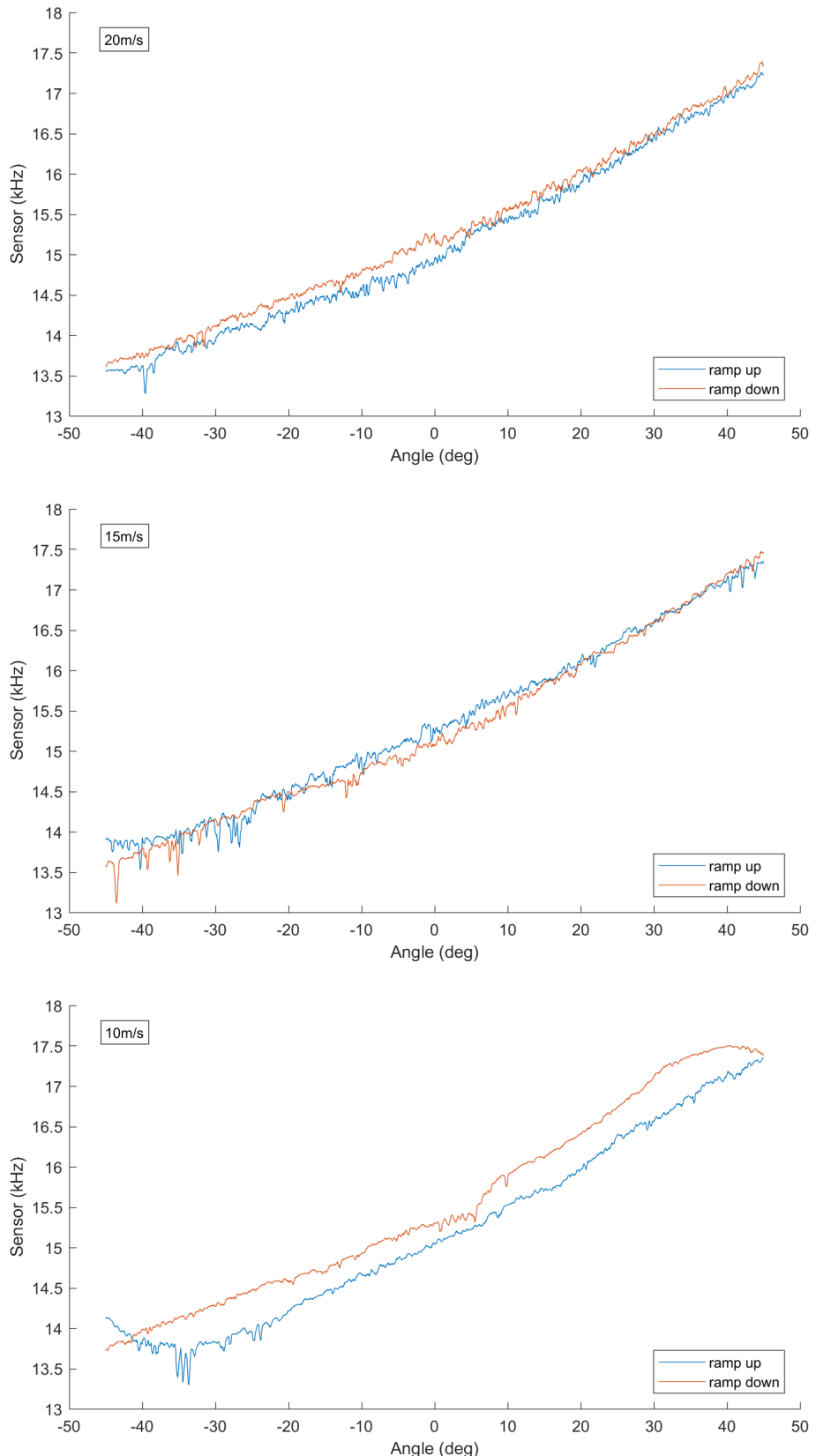


Figure 4.22: Capacitive sensor - wind-tunnel calibration (20m/s, 15m/s, 10m/s)

The above figures show reasonably low noise across all airspeeds. Some offset between the rising and falling curve of the ramp response in the 20m/s and 15m/s figure can be noticed. Since the offsets invert between the two airspeeds, it is assumed that they are not due to hysteresis in the sensor, but possibly due to the drift problem. On the other hand, the 10m/s clearly shows some hysteresis, presumably due to the friction on the variable capacitor core. It matches the observation that the capacitive sensor has less friction than the resistive sensor, but more than the magnetic sensor.

With the function described in section 3.4 a calibration curve can be generated. Most of the constants in that formula are unknown. For this reason, the formula is written in a more general form  $\alpha(v) = (C_1v + C_2)/(C_3v + C_4)$  where  $C_1 \dots C_4$  are complicated functions of the constants. A least-square fit with that general function for the 20m/s and 15m/s curves produces practically the same result:  $\alpha(v) = (0.0187v - 352.3871)/(0.0001v - 0.3641)$  with a root-mean-square error of 1.2° for 20m/s and 2.0° for 15m/s (1.6° over both). The circumstance that both airspeeds have the same calibration curve although the drift problem could have caused an offset between the two is regarded as a random coincidence. A calibration curve for 10m/s airspeed is not done because of the hysteresis.

### System Identification

The system identification of the capacitive sensor was performed regardless of the problems described above. A first-order system is used to identify a time constant respectively corner frequency. Each step/chirp response is normalised separately because no calibration curve is available. This leaves the possibility open that the hysteresis skews the results for the 10m/s airspeed measurements.

Table 4.4 shows the time constant of a first-order system fitted to the step responses of the sensor. The corresponding fit quality is noted in parentheses beside it. This is listed for all three airspeeds and for five reference angles. It shows significant differences between reference angles and airspeeds. It appears that lowering airspeeds and lowering reference angles correspond to raising time constants.

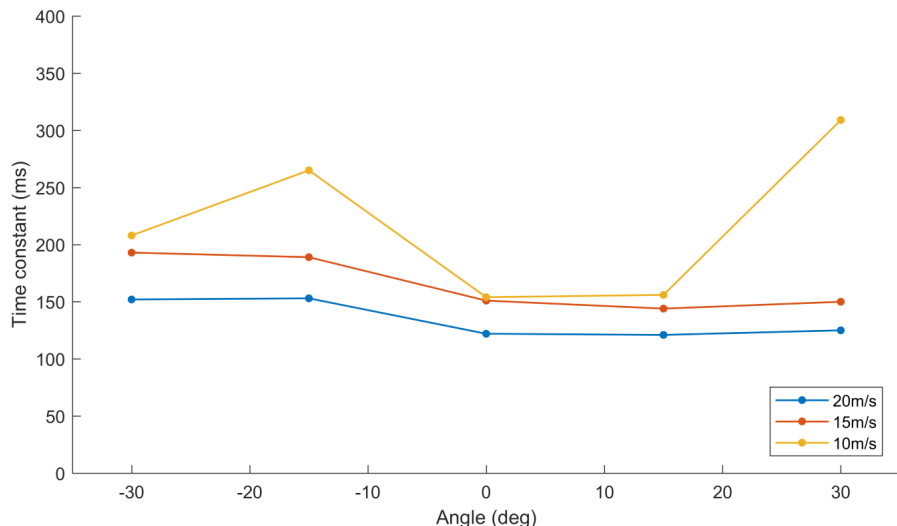


Figure 4.23: Capacitive sensor - plot of table 4.4

	-30°	-15°	0°	15°	30°
20m/s	152ms (81%)	153ms (80%)	122ms (83%)	121ms (80%)	125ms (80%)
15m/s	193ms (83%)	189ms (83%)	151ms (81%)	144ms (81%)	150ms (84%)
10m/s	208ms (71%)	265ms (81%)	154ms (75%)	156ms (70%)	309ms (71%)

Table 4.4: Capacitive sensor - time constants for different angles and airspeeds

For the capacitive sensor, like for the other two, the upper frequency limit of the chirp signal ( $f_{end} = 3\text{Hz}$ ) is not high enough to be useful for system identification as the relevant dynamics happen at higher frequencies.

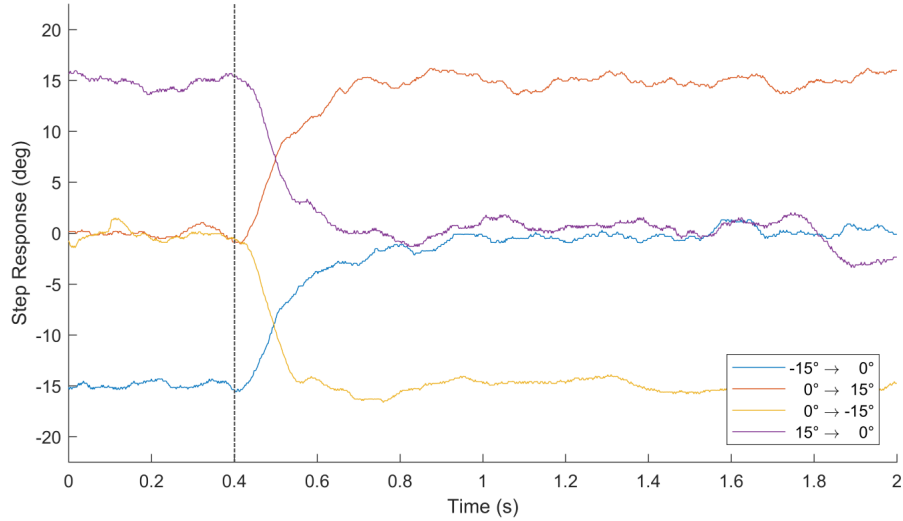


Figure 4.24: Capacitive sensor - step responses at 0°, 20m/s

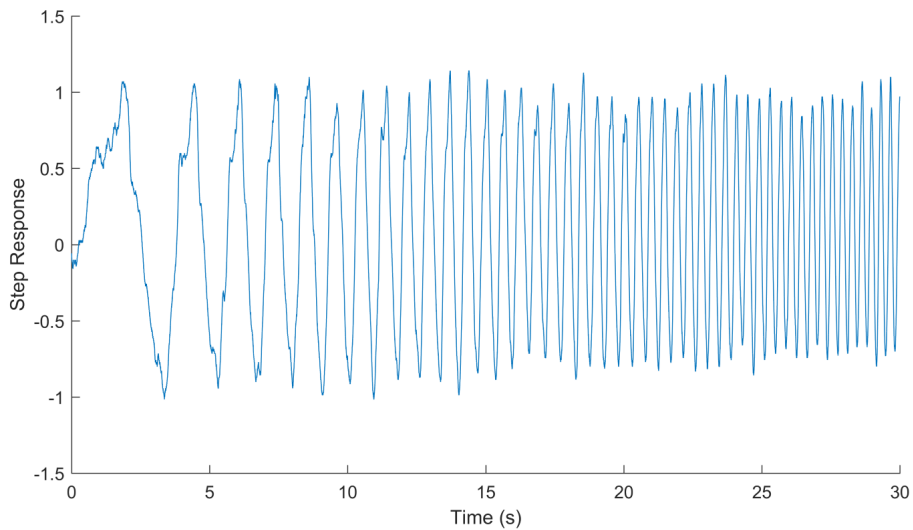


Figure 4.25: Capacitive sensor - chirp responses at 0°, 20m/s

## Chapter 5

# Summary and Outlook

In summary out of the many possible angle of attack sensor designs three were chosen for this thesis to be analysed based on chances of success. The three were all vane-type sensors that have a little wing that aligns itself with the airflow and moves a rotary encoder that in turn outputs a measurement of the angle of attack. The three designs differ in the type of rotary encoder which is used. The first uses a potentiometer (resistive sensor), the second a combination of magnet and Hall effect sensor (magnetic sensor) and the third a variable capacitor in combination with a 555 timer circuit (capacitive sensor).

All sensors were developed in parallel and the developing effort was subdivided based on the apparent performance (investing more in the ones that performed worse). The following conclusions can be made for the three designs:

### **Resistive Sensor:**

- 11.70 CHF / 9 g
- + Easy to manufacture with low number of components
- + Simple reading through ADC
- Hysteresis is present due to high friction at 15m/s airspeed ( $10^\circ$  to  $30^\circ$ )
- Sensor is inoperative due to high friction at 10m/s airspeed

### **Magnetic Sensor:**

- 13.10 CHF / 8 g
- + Simple reading through ADC
- + No detectable hysteresis ( $< 1^\circ$ )
- + No detectable delay ( $< 2ms$ )
- Prone to oscillation of the vane (amplitude  $\approx 4^\circ$  in wind-tunnel)

### **Capacitive Sensor:**

- 13.20 CHF / 16 g
- Complex design and difficult to fine-tune
- Has problems with measurement-drift over time (up to  $1^\circ/min$ )
- Hysteresis is present due to friction at 10m/s ( $\approx 10^\circ$ )

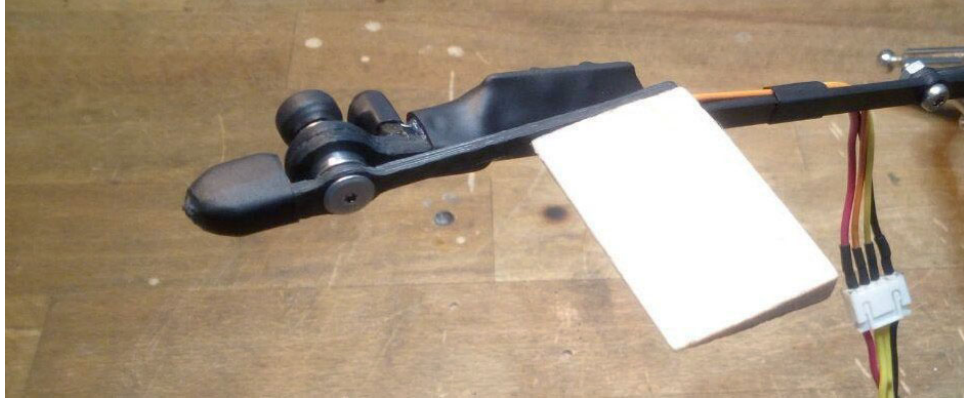


Figure 5.1: Magnetic sensor - version 2

Out of the three sensors, the magnetic one seems to be the most promising for further development. A last version of this design was built to see if the oscillation problem could be solved. Starting from the earlier design described in section 3.3 the following changes were made: Addition of a second bearing, shortening of the swing-arm with addition of more counterweight, alteration of the vane shape to a wedge, putting of an ADC directly behind the Hall effect sensor. All the possible factors that could contribute to the oscillation are covered by these modifications (as described in 4.3), except for the possibility that the wind-tunnel itself produces a turbulent airflow.

The results from the wind-tunnel tests show nearly the same exact responses as with the previous version. The calibration curve is slightly different due to the manufacturing process, but the oscillation of the vane is still identical. This indicates that the oscillation is caused by the wind-tunnel and not a design error in the sensor. In-flight data of the first and second version of the magnetic sensor (Figure 5.2) further confirm this assumption as they do not show any oscillation in the determined frequencies and amplitudes.

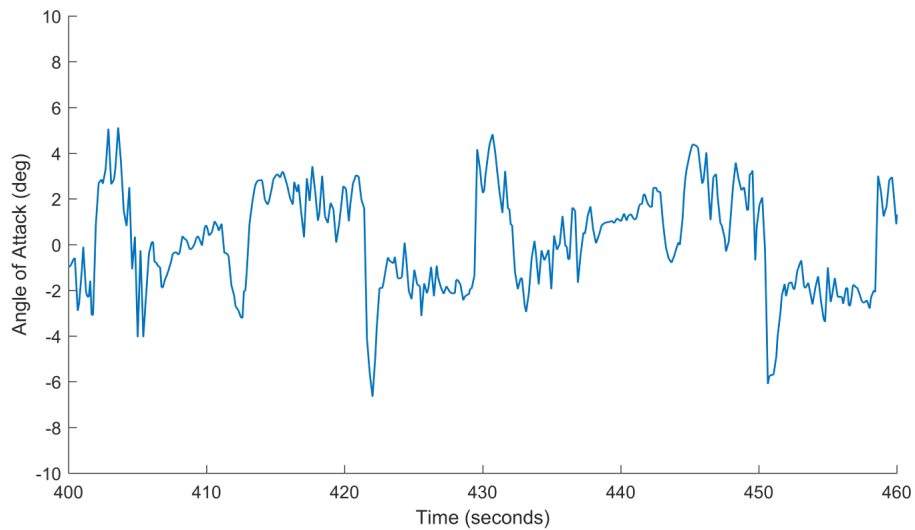


Figure 5.2: Magnetic sensor v2 - in-flight angle of attack

# Bibliography

- [1] Angle of attack. [en.wikipedia.org/wiki/angle\\_of\\_attack](https://en.wikipedia.org/wiki/angle_of_attack).
- [2] Nasa aeronautics guided tour. [www.grc.nasa.gov/www/k-12/airplane/incline.html](http://www.grc.nasa.gov/www/k-12/airplane/incline.html).
- [3] Nasa lift coefficient. [www.grc.nasa.gov/www/k-12/airplane/liftco.html](http://www.grc.nasa.gov/www/k-12/airplane/liftco.html).
- [4] W. Gracey, *Summary of Methods of Measuring Angle of Attack on Aircraft*. Langley Aeronautical Laboratory, 1958.
- [5] Rotary encoder. [en.wikipedia.org/wiki/Rotary\\_encoder](https://en.wikipedia.org/wiki/Rotary_encoder).
- [6] A. J. Fleming, *A review of nanometer resolution position sensors: Operation and performance*. School of Electrical Engineering and Computing Newcastle, 2013.
- [7] A. M. Mujahid Abdulrahim and S. Watkins, *Control Strategies for Flight in Extreme Turbulence*. RMIT University, Melbourne, VIC, Australia, 2017.
- [8] J. Oehler, *Measuring apparent flow vector on a flexible wing kite*. University of Stuttgart Stuttgart Wind Energy (SWE), 2017.
- [9] *Simple DIY Angle of Attack (AoA) Indicator*. AKAFlieg Graz.
- [10] E. J. Montoya, *Wind-Tunnel Calibration and Requirements for In-Flight use of fixed hemispherical Head Angle-of-Attack and Angle-of-Sideslip Sensors*. Flight Research Center Edwards, Calif., 1973.
- [11] B. A. S. P. M. Ligrani and L. R. Baun, *Miniature five-hole pressure probe for measurement of three mean velocity components in low-speed flows*. Journal of Physics E: Scientific Instruments, 1989.
- [12] Amtek angle of attack transducer. [www.ameteksfms.com/-/media/ameteksensors/documents/sensor%20data%20sheets/angle-of-attack.pdf](http://www.ameteksfms.com/-/media/ameteksensors/documents/sensor%20data%20sheets/angle-of-attack.pdf).
- [13] S. Callegari, *Aircraft Angle of Attack and Air Speed Detection by Redundant Strip Pressure Sensors*. ARCES/DEIS, University of Bologna, 2004.
- [14] List of dielectric constants. [www.vega.com/-/media/PDF-files/List\\_of\\_dielectric\\_constants\\_EN.ashx](http://www.vega.com/-/media/PDF-files/List_of_dielectric_constants_EN.ashx).
- [15] Coefficients of friction. [http://www.roymech.co.uk/Useful\\_Tables/Tribology/co\\_of\\_frict.htm](http://www.roymech.co.uk/Useful_Tables/Tribology/co_of_frict.htm).

## **Appendix A**

### **Tools which were used**

- CNC Router - Shapeoko 3
- Soldering Station - Hakko FX-951
- Third hand, Flux, Lighter , Magnifying glass
- Multimeter - Fluke 12E+
- Caliper, Ruler
- Hot glue gun
- Tweezers, Pliers, Probes
- Cutters, Scalpels, Files
- Screwdrivers
- (Crimping Tools)
- (Oscilloscope - Picoscope 2204A)